

Tracing 3D Anatomy in 2D Strokes: A Multi-Stage Projection Driven Approach to Cervical Spine Fracture Identification

Fabi Nahian Madhurja^{1,‡}, Rusab Sarmun^{2,‡}, Muhammad E. H. Chowdhury^{3,*}, Adam Mushtak⁴, Israa Al-Hashimi⁴, Sohaib Bassam Zoghoul⁴

¹Department of Computer Science and Engineering, Brac University, Bangladesh. Email: fabinahian@gmail.com (FNM)

²Department of Electrical and Electronic Engineering, University of Dhaka, Bangladesh. Email: rusabsarmun@gmail.com (RS)

³Department of Electrical Engineering, Qatar University, Doha 2713, Qatar. Email: mchowdhury@qu.edu.qa (MEHC)

⁴Department of Radiology, Hamad Medical Corporation, Doha, Qatar. Email: adamrads94@gmail.com (AM), ialhashimi@hamad.qa (IAH), sohaibzoghoul@gmail.com (SBZ),

*Correspondence: Muhammad E.H. Chowdhury (mchowdhury@qu.edu.qa).

‡ These authors contributed equally to the work

Abstract

Cervical spine fractures are critical medical conditions requiring precise and efficient detection for effective clinical management. This study extensively explores the viability of 2D projection-based vertebra segmentation for vertebra-level fracture detection in 3D CT volumes, presenting an end-to-end pipeline for automated analysis of cervical vertebrae (C1–C7). By approximating 3D volume through optimized 2D axial, sagittal, and coronal projections, regions of interest are identified using the YOLOv8 model from all views and combined to approximate the 3D cervical spine area, achieving a 3D mIoU of 94.45%. This projection-based localization strategy reduces computational complexity compared to traditional 3D segmentation methods while maintaining high performance. It is followed by a DenseNet121-Unet-based multi-label segmentation, leveraging variance and energy-based projections, achieving a Dice score of 87.86%. Strategic approximation of 3D vertebral masks from these 2D segmentation masks enables the extraction of individual vertebrae volumes. The volumes are then analyzed for fractures using an ensemble of 2.5D Spatio-Sequential models, incorporating both raw slices and projections per vertebra for complementary evaluation. This ensemble achieves vertebra-level and patient-level F1 scores of 68.15 and 82.26, and ROC-AUC scores of 91.62 and 83.04, respectively. We further validate our approach through an explainability study, which provides saliency map visualizations to highlight the anatomical regions the model focuses on for diagnosis, and an interobserver variability analysis, which compares our model's performance with expert radiologists, demonstrating competitive results.

Keywords: Cervical spine fracture detection; 2D projection-based analysis; Vertebra segmentation; Deep learning in CT imaging; Multi-stage medical image analysis

1. Introduction

Cervical spine fractures present an important clinical concern, with potentially life-threatening consequences for affected individuals, as they can cause severe damage to the spinal cord [1]. The cervical spine, anatomically positioned within the neck, is the top-most segment of the vertebral column. It consists of seven distinct vertebrae C1 through C7, extending from the base of the skull to the thoracic spine. The first cervical vertebra (C1, or atlas) is connected with the occipital bone of the skull, while the second vertebra (C2, or axis) includes specialized structures that enable axial rotation. Vertebrae C3 through C6 are considered "typical" vertebrae, exhibiting shared morphological features such as vertebral bodies, pedicles, and facet joints. The seventh vertebra (C7, or vertebra prominens) serves as a transition between the cervical and thoracic regions [2]. Together with intervertebral discs, ligaments, and musculature, these vertebrae provide structural support, facilitate a wide range of head and neck motion, and, most critically, protect the cervical segment of the spinal cord [3, 4]. **Figure 1** shows the anatomical structure of the cervical spine and the atypical cervical vertebrae. Given this complex anatomy and functional importance, trauma to the cervical spine can have profound neurological implications. These injuries are frequently caused by high-energy mechanisms, such as falls or vehicular collisions and are associated with high morbidity and mortality rates [5]. In North America alone, cervical spine injuries account for more than one million clinical cases annually [6]. If not diagnosed and managed promptly, such injuries can lead to permanent neurological deficits,

including paralysis or death [7-9]. Therefore, timely and accurate diagnosis is crucial to guiding treatment decisions and improving patient outcomes [10, 11].

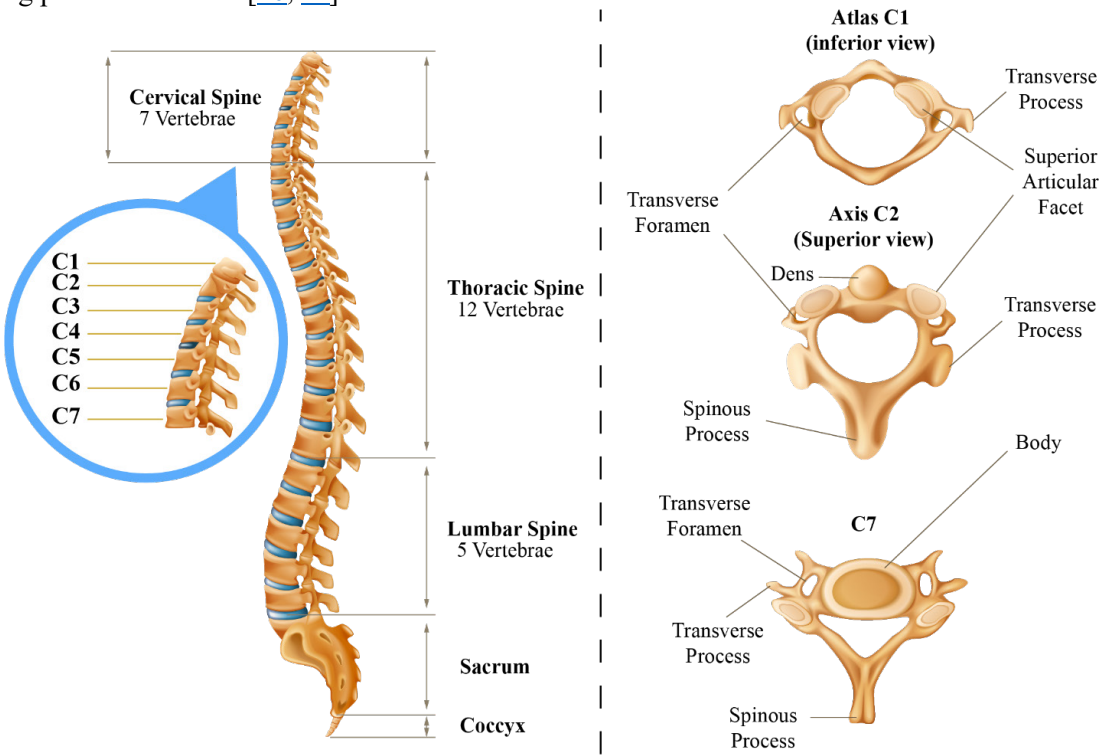


Figure 1 Anatomical structure of the spine and atypical cervical vertebrae

Computed Tomography (CT) is the primary imaging modality for assessing suspected cervical spine trauma, due to its high spatial resolution and diagnostic reliability [12]. Nevertheless, CT interpretation remains a nontrivial task. The volumetric nature of CT data, especially with high-resolution acquisitions, results in a substantial number of slices that must be reviewed manually, imposing a significant burden on radiologists and increasing the likelihood of fatigue-related errors [13-16]. Additional diagnostic complexity arises from overlapping degenerative changes and anatomical variability, which can obscure fracture visualization and contribute to missed or delayed diagnoses [17].

In response to these challenges, artificial intelligence (AI) and deep learning (DL) methods have gained traction as tools for automating diagnostic tasks and supporting clinical decision-making [18, 19]. In cervical spine imaging, these approaches can improve the speed, accuracy, and consistency of fracture detection while alleviating radiologist workload [20, 21]. However, while many existing AI models rely on either full 3D CT volumes or 2D slice-wise analysis, both modalities present limitations: the former demands substantial computational resources, whereas the latter may lack sufficient spatial context for accurate fracture detection while workflows involving direct 3D analysis are computationally intensive [22], and many AI models in the literature have been trained on balanced datasets, which do not reflect real-world class imbalances, thereby limiting their generalizability.

This study investigates the feasibility of using 2D projections derived from 3D CT volumes for vertebra-level cervical spine fracture detection. Specifically, we propose a novel end-to-end pipeline that integrates object detection, segmentation, and classification within a mostly projection-based framework. The pipeline first employs YOLOv8 [23] to localize the cervical spine across axial, sagittal, and coronal projections. A Unet-based architecture is then used to perform multi-label segmentation of individual vertebrae (C1–C7) using optimized variance and energy-based projections. The segmented vertebral volumes are subsequently evaluated for fractures using a wide array of techniques utilizing both projection and slice-wise information. Additionally we propose an ensemble-based 2.5D spatio-sequential model that performs comparably to 3D segmentation-based methods for vertebra-level fracture recognition. One of the main objectives of the study is to explore whether optimized 2D projections, in

conjunction with object detection models, can provide a computationally efficient method specifically for cervical spine localization, whether multi-label segmentation on selected 2D views can accurately approximate 3D vertebral masks, and whether that estimated vertebral volume is viable for high vertebra and patient-level fracture diagnostic performance. Furthermore, to validate the clinical viability and trustworthiness of this approach, the study incorporates a comprehensive explainability analysis, which provides saliency map visualizations to highlight the anatomical regions the model focuses on for diagnosis, and an interobserver variability analysis. This latter analysis compares the model's performance with that of three expert radiologists, revealing that the model shows comparable performance.

In this study, our main contributions are as follows:

- Development of an end-to-end pipeline for automated cervical spine fracture detection leveraging 2D projections for localization and segmentation.
- A novel application of multi-label segmentation on multiple optimized 2D projections to approximate 3D masks for individual vertebrae (C1–C7).
- An ensemble of 2.5D Spatio-Sequential models, integrating complementary information from both slice stacks and projection stacks derived from approximated vertebra volumes, for robust fracture classification.
- Comprehensive investigation and selection of optimal mathematical projection techniques for different stages of the pipeline.
- An elaborate interobserver variability study comparing model performance with three expert radiologists.
- To the best of our knowledge, this is the first work to extensively investigate the viability of projection-based segmentation for fracture classification.

The remainder of this paper is organized as follows. Section 2 provides a comprehensive review of related work, highlighting existing approaches to cervical spine fracture detection and relevant developments in deep learning for medical imaging. Section 3 outlines the proposed methodology, including details of the dataset, data preprocessing, model architectures, and evaluation metrics. Section 4 presents the experimental results and compares the performance of the proposed pipeline against baseline detection models. Section 5 discusses the limitations of the current study and outlines potential directions for future research. Finally, Section 6 concludes the paper with a summary of key findings and contributions.

2. Related Works

Generally, radiologists visually inspect MRI or CT slices to identify spine fractures. With the advent of artificial intelligence and deep learning, several studies have explored automated spine fracture detection, where Convolutional Neural Networks (CNN) play a central role. Small et al. used C spine, a Food and Drug Administration (FDA) approved CNN, on a private dataset of 665 examinations and achieved 92% accuracy and 76% sensitivity [24]. Esfahani et al. applied a CNN based system on a subset of 4050 images from a public dataset and reported 100% accuracy, although this was obtained on a balanced subset that does not reflect real world class imbalance [25]. A 3D CNN based study reported vertebra level and patient level fracture prediction on only 14 patients, achieving 14% accuracy [3]. Nicolaes et al. implemented a voxel wise 3D CNN on 90 cases and reported AUC scores of 95 and 93 for patient level and vertebra level fracture detection, respectively [26]. Other work has used pretrained backbones such as MobileNetV2 [27] with custom layers for real time CT based fracture detection on a balanced subset of 4200 images from the RSNA 2022 Cervical Spine Fracture dataset [28], which again does not represent clinical class imbalance [29]. Mahajan et al. explored sagittal and coronal slices with custom CNNs but achieved sub optimal accuracies of 51.88% and 53.19% compared to 55.58% for axial slices [30]. Chen et al. used a 3D V-Net for vertebral body segmentation in thoracolumbar compression fractures (Dice Similarity Coefficient 90%) and ResNet18 for classifying fresh versus old fractures, with AUCs of 0.96 (internal), 89 (external), and 87 (prospective) [31].

Some studies have incorporated state-of-the-art object detection models for fracture or vertebra localization. Gaikwad et al. combined YOLOv5 [32] for spine localization with a DenseNet201-based classifier [33] for fractured slice detection, achieving an AUC of 94% and sensitivity of 86% [4]. Chlad et al. proposed a cloud based system

using YOLOv5 for vertebra region of interest (ROI) detection and a ViT based classifier [34] for fractured slices; on an undersampled balanced subset of the RSNA dataset [28], DeiT-T16 achieved 98% accuracy, and the system notified clinicians when a fracture was suspected [35]. Nejad et al. used a Global Context ViT for C1–C7 vertebra classification from CT slices with image and meta data input, followed by YOLOv8 [23] for fracture detection, achieving an mAP50 of 96% on the 12% of RSNA data with bounding box annotations [36]. Boonrod et al. evaluated YOLOv2–YOLOv4 on 229 sagittal radiographs, achieving 80% accuracy and 72% sensitivity, and compared performance against radiologists, residents, and orthopedists [37]. Another two stage framework used YOLOv8 for C1–C7 vertebra detection and a custom CNN for fracture classification, with Grad CAM [38] for explainability; trained on a strategically undersampled balanced subset of the RSNA dataset, it achieved an mAP of 93.5 for vertebra identification and an F1 score of 97.8% [39]. Golla et al. proposed a multi stage framework that combines segmentation and fracture detection. Using 374 cases from the VerSe dataset, a Fovea network first produced coarse segmentation to localize vertebrae, and a Unet [40] then performed fine segmentation and fracture detection in multiple representations, with the Volume of Interest (VOI) based approach detecting 87.2% of fractures at 3.5 false positives per case on a private dataset of 195 scans [20]. Sutradhar et al. developed a two stage system with VertNet 10, a custom CNN with attention for vertebra classification, and a modified YOLOv8 for fracture localization, achieving an mAP of 93 [18].

Sequential models have also been explored for fracture detection. In order to detect osteoporotic vertebral fractures (OVF), Tomita et al. used a CNN LSTM strategy for osteoporotic vertebral fracture (OVF) detection, where a deep CNN extracted features from the middle 5% sagittal slices and an LSTM aggregated them across the scan, achieving 89.2% accuracy and 90.8% F1 score at patient level on 1432 scans [41]. Salehinejad et al. proposed a CNN LSTM model on 3666 cases, using a 3D ResNet50 for feature extraction and a bidirectional LSTM for fracture prediction with saliency maps, and stacking gross bone, standard bone, and soft tissue windows in three channels. With 7 fold cross validation, they reported an average F1 score of 52.92 and AUC of 71.57 at patient level, while slice level performance remained low (F1 11.92 and AUC 77.42) [42]. Hung et al. employed a 2.5D CNN that takes eight stacks of three slices per vertebra to jointly classify C1–C7 vertebrae and predict bounding boxes, followed by ROI cropping and a second 2.5D CNN with bidirectional LSTM aggregation. Trained with 5 fold cross validation on the RSNA challenge data, the model achieved log losses of 0.2115 and 0.2389 on public and private test sets, although clinically oriented metrics such as F1 and AUC were not reported [19]. Kim et al. combined a 3D EfficientNet B5 Unet for C1–C7 segmentation (reported Dice score 1.00), YOLOv5 for spinal column ROI localization, and a CrackNet LSTM for fracture detection, achieving 94.9% accuracy [43].

While some studies like Kim et al. and Golla et al. have focused on segmentation as a critical preprocessing step for vertebra fracture identification and localization, segmentation of spinal structures are more broadly addressed in other dedicated studies. One work proposed an iterative fully convolutional network (FCN) for vertebra segmentation and identification in 3D CT and MR images, using a memory mechanism for instance wise segmentation and sequential labeling, and reporting an average Dice score of $94.9\% \pm 2.1\%$ [44]. The Spine Transformers framework addressed vertebra labeling and segmentation in arbitrary field of view CT scans with a 3D transformer based object detector and a multi task encoder decoder network, achieving an Id Rate of 97.22% and DOC of 0.911 on the VerSe 2019 public test set [45, 46]. Mao et al. introduced the Semantics and Instance Interactive Learning (SIIIL) framework with the MILL and OCPL modules for vertebra labeling and segmentation in 3D CT, achieving an identification rate of 96.61% and Dice of 94.07% on CTSpine1K [47, 48]. Kawathekar et al. (2024) presented a fully automated pipeline combining Unbalanced Unet for spine localization, 3D SpatialConfiguration Net (SCN) for vertebra labeling, and 3D U Net for segmentation, reaching Dice scores of 93.07% and 92.01% [49]. The Atrous ResUnet framework proposed an encoder decoder strategy with Atrous Residual Path, 3D Attention Module, and Layer Normalization [50] and obtained a Dice coefficient of 89.28% on the CSI 2014 dataset [51, 52]. The SVseg model, based on a stacked sparse autoencoder and sigmoid classifier, achieved a Dice of 87.39% and Jaccard of 77.60% on the MICCAI CSI dataset [53]. A two stage Dense U Net approach used a 2D Dense U Net for vertebral centroid detection and a 3D Dense U Net for instance segmentation, achieving a Dice of 0.953 and a 100% detection rate on CSI 2014 [54]. Han et al.’s Spine GAN framework combined atrous convolution, local LSTM, and a discriminative network for simultaneous segmentation and classification of spinal structures in MRI, achieving a Dice of 87.1% on 253 patients [55]. Wu et al. proposed the three stage LVLS HVPFE framework, which uses hybrid sagittal and coronal projection images, a 2D projection

location network, 3D localization via the Spatial Dimensionality Reduction Localization Criterion (SDRLC), and a Unet3D inspired network, achieving an average Dice of 94.9% [56].

As detailed in **Supplementary Table S1**, most existing work reported slice-level metrics or evaluated on balanced test sets that do not capture the severe class imbalance in real world trauma populations, and many approaches rely on computationally intensive full 3D or slice wise processing, limiting clinical scalability. In response, our study introduces a pipeline that prioritizes efficient anatomical localization by leveraging optimized 2D projections to approximate 3D anatomy, using only two to three projections per patient to reduce computational overhead while preserving diagnostic performance.

Unlike previous studies that mainly use projections for vertebra identification, direct segmentation on projections to estimate 3D masks has not been systematically investigated. To the best of our knowledge, our work is the first to assess projection-based segmentation for fracture classification. We extend the CNN LSTM paradigm by introducing an ensemble of 2.5D Spatio-Sequential CNN Transformer models that integrate complementary information from axial slices and projection stacks. This framework is rigorously evaluated with 5-fold cross validation on the full, imbalanced dataset. In addition, we support clinical interpretability through Grad CAM visualizations and assess reliability via an interobserver variability study, demonstrating performance competitive with three expert radiologists.

3. Method

In our study, cervical spine fracture detection from 3D CT volumes was done by leveraging 2D projection-based techniques to address the computational challenges of traditional 3D methods. In our three step process, at first, 2D axial, sagittal, and coronal projections were generated from the 3D volume created from the provided DICOM files. A spine column VOI had been approximated from the multi-view ROIs identified using the YOLOv8 model from the aforementioned projections. A Unet-based multi-label segmentation was then applied to generate 2D masks of each vertebra from the sagittal and coronal projection of the spine column VOI, which were combined to reconstruct 3D vertebral masks and extract individual vertebrae volumes. Finally, these volumes were analyzed for fractures using an ensemble of two 2.5D CNN-Transformer models. A bird's-eye view of our pipeline is shown in **Figure 2**.

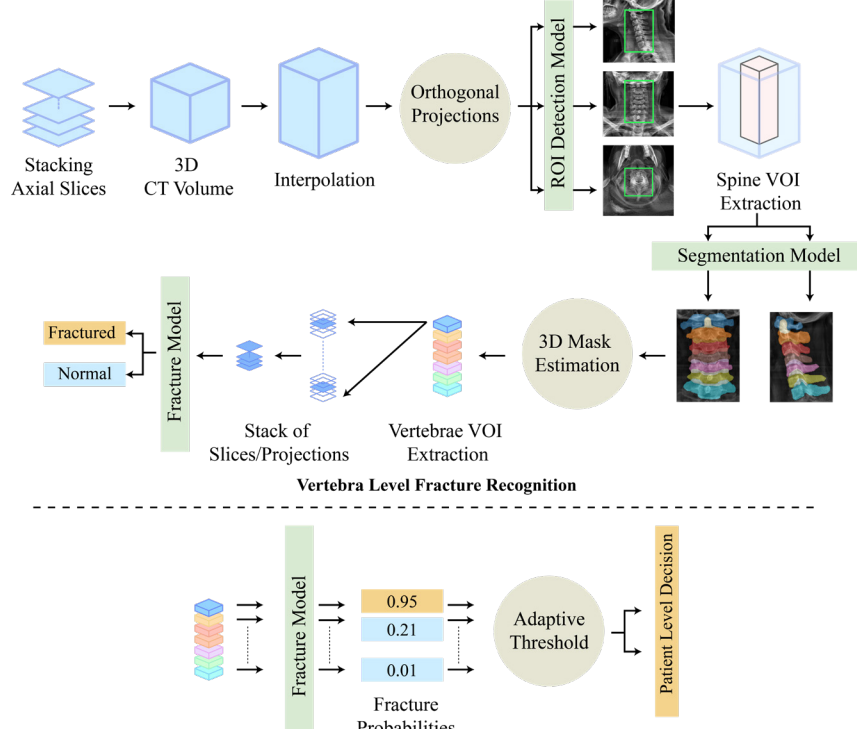


Figure 2 Methodology Overview

3.1. Dataset Description

Our research utilized the public training set of the RSNA Cervical Spine Fracture Challenge 2022. The dataset consisted of CT scans from 2019 patients, of which 961 had at least one fractured cervical vertebra. The dataset included strict inclusion criteria, specifically requiring axial non-contrast CT scans with 1mm slice thickness. Each patient's CT volume consisted of an average of 350 slices. Bounding box fracture annotations had been given for 235 patients, and voxel-level 3D segmentation masks were given for 87 patients. The segmentation data was given as Neuroimaging Informatics Technology Initiative (NIIfTI) files that labels cervical vertebrae C1-C7 (values 1-7) and thoracic vertebrae (values 8-19), with background labeled as 0. Data collection was performed by 12 institutes from 6 continents making it one of the largest publicly available cervical spine fracture datasets. The fracture distribution in the dataset is highly imbalanced and reflects real-world clinical scenarios, with C2, C6, and C7 being the most frequently fractured vertebrae. It is important to note that the dataset treats acute and chronic fractures equivalently and excludes post-surgical cases due to challenges associated with streak artifacts and altered anatomy[28]. Fracture distribution statistics and sample CT slices are provided in **Supplementary Figure S1**.

3.2. 2D Projections of 3D CT Volume

To address the challenges of analyzing 3D CT volumes computationally, we employed 2D projection techniques that distill volumetric data into informative 2D representations. Orthogonal projections are computational techniques applied to volumetric imaging data such as CT to visualize the voxel intensities along specific views like axial, sagittal and coronal. Usage of different kinds of projection methods or functions enhances different anatomical features of the volume, the most popular of which is Maximum Intensity Projection (MIP) [57] for analysis of CT volumes. It highlights maximum intensity pixels along the viewing direction, which is essentially a method of summarizing the volumetric data into a 2D plane. This summarization can be done using any function creating different projections. In this study, we have done an extensive investigation on several projection methods and their utility in cervical spine localization and vertebra segmentation. We have analyzed projections for both ROI detection and segmentation phases of the study and based on our investigation, we adopt variance projection for cervical spine ROI localization and energy projection for vertebra segmentation, as these projections were found to best preserve task-specific anatomical characteristics while maintaining computational efficiency.

Let $I(x, y, z)$ denote the voxel intensity at spatial location (x, y) in slice z , and let Z be the total number of slices along the projection axis. The variance projection is defined as:

$$P_{\text{var}}(x, y) = \frac{1}{N} \sum_{z=1}^N (I(x, y, z) - \mu(x, y))^2 \quad (1)$$

where $\mu(x, y) = \frac{1}{N} \sum_{z=1}^N I(x, y, z)$ represents the mean intensity along the projection axis. This projection emphasizes regions with high intensity variability across slices, resulting in strong contrast between vertebral structures and surrounding soft tissue. Such characteristics make variance projection particularly suitable for robust localization of the cervical spine region of interest.

For vertebra segmentation, we employ the energy projection[58], defined as:

$$P_{\text{eng}}(x, y) = \sum_{z=1}^N I(x, y, z)^2 \quad (2)$$

Energy projection amplifies high-intensity anatomical structures, such as cortical bone, and enhances vertebral boundaries that are critical for accurate segmentation. This property is especially beneficial when generating projection-based representations for multi-label vertebra segmentation under anatomical overlap. Representative examples of variance and energy projections derived from the same cervical spine CT volume are shown in **Figure 3**, illustrating their complementary characteristics for ROI localization and vertebra segmentation, respectively.

Comprehensive description of alternative projection operators, including their mathematical formulations and visual comparisons, are provided in the **Supplementary Section S3**.

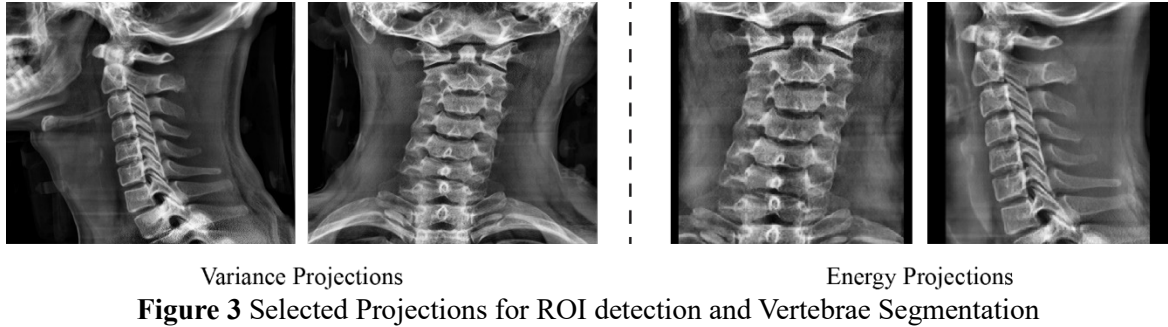


Figure 3 Selected Projections for ROI detection and Vertebrae Segmentation

3.2.1 Slice interpolation

CT volumes in the RSNA dataset exhibit substantial variability in the number of axial slices per patient, ranging from fewer than 200 to more than 500 slices. For scans with sparse sampling, vertebral structures may be underrepresented in projection space, negatively affecting downstream localization and segmentation performance. To mitigate this issue and ensure consistent volumetric resolution across patients, we apply slice interpolation as a preprocessing step.

CT volumes were interpolated using cubic spline interpolation [59] to preserve anatomical continuity and reduce high-frequency artifacts, while segmentation masks were interpolated using nearest-neighbor interpolation to maintain label integrity. After interpolation, all volumes contained at least 400 slices, ensuring comparable anatomical coverage across the dataset. **Figure 4** demonstrates an example of the projection with and without interpolation for the CT volume and its corresponding mask. It is clearly observed that the projection with the interpolation showed more distinct vertebra features. Hence, this preprocessing step improved the clarity and structural consistency of projection-based representations, particularly for low-slice scans

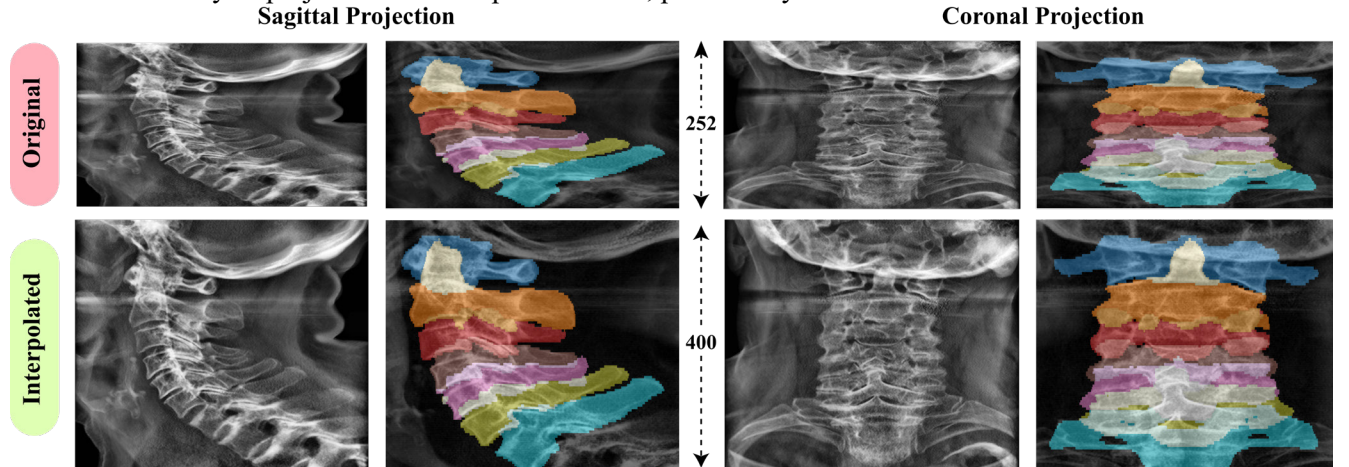


Figure 4 Interpolation of slices

3.3. Cervical Spine VOI Detection

The CT scans of the patients contained regions other than the cervical spine. So, it was crucial to localize and separate the cervical spine region from the whole volume for subsequent steps to focus more on the ROI. This makes it easier for the segmentation model to segment the individual cervical vertebra without being distracted by the thoracic ones. The dataset provided 87 patients with 3D vertebra mask. One of the goals of our project was to effectively utilize 2D projection-based methods to estimate vertebra locations in the 3D volume and use that information for vertebra-level fracture identification. We utilized projections from all 3 views and their masks to estimate the cervical spine region by utilizing a YOLO based system.

3.3.1 Bounding box generation from 3D mask data

The dataset included annotations for cervical vertebrae (C1–C7) and thoracic vertebrae (T8–T19). To focus exclusively on the cervical spine, the labels for C1–C7 were isolated and combined to construct a binary mask representing the cervical region. This 3D binary mask was then processed using max projection, resulting in 2D projections from the coronal, sagittal, and axial views. To accurately localize the ROI, a bounding box was mathematically computed for each 2D projection by identifying the highest and lowest x and y coordinates of the largest connected component in the mask. This ensured that the bounding box precisely encompassed the mask while ignoring smaller, isolated fragments, thereby eliminating imperfections in the ground truth. The process of generating ground truth bounding boxes is illustrated in **Figure 5**.

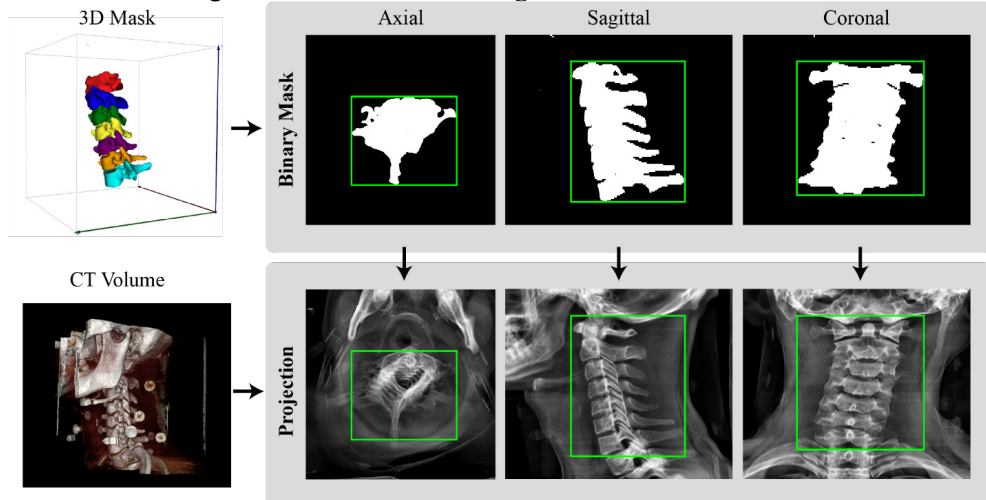


Figure 5 2D ROI Bounding box calculation from 3D mask

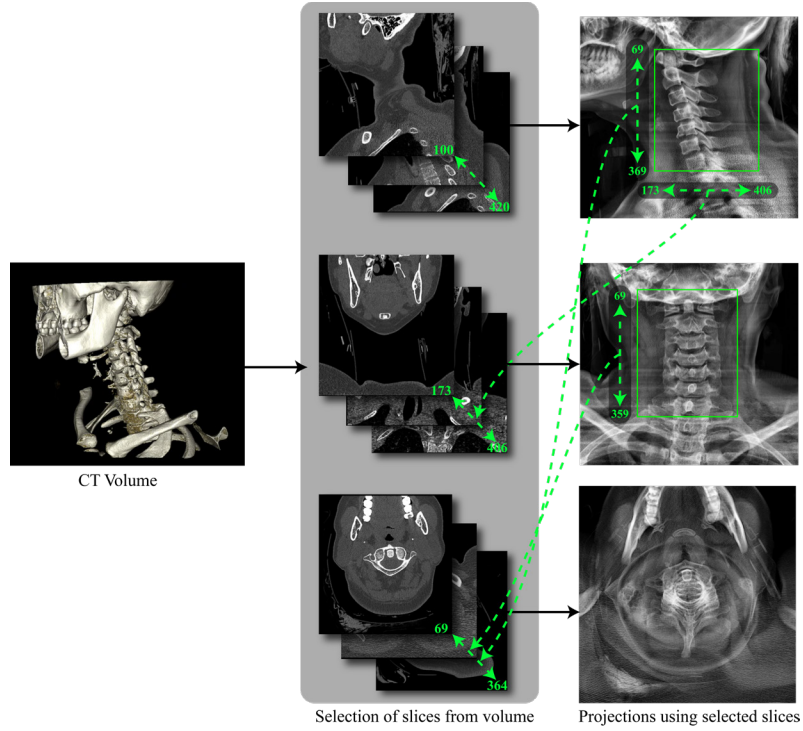


Figure 6 Slice selection process

3.3.2 Sequential Slice Selection

To obtain the most accurate projection, it is essential to select slices that exclusively encompass the cervical spine. Therefore, a sequential slice selection approach was developed to achieve this efficiently. Initially, the bounding boxes for the given 87 patients were visualized. A common region in the center was identified based on where those 87 bounding boxes were. The upper and lower x-coordinates of these bounding boxes were identified, and a few outliers were excluded. These heuristically determined coordinates served as the baseline for all patients and were utilized to refine the sagittal selection. A sagittal slice range of 100–420 was selected for sagittal projection generation. A visual example of this heuristic sagittal selection is provided in **Supplementary Figure S7**.

Afterwards, the width of the sagittal bounding box for each patient was utilized to identify the corresponding coronal slices to generate a refined coronal projection. And finally, the axial slice range for a refined axial projection was determined by averaging the heights of the coronal and sagittal bounding boxes for each patient. This process is demonstrated with an example in **Figure 6**. The figure shows that at first the 100–420 slice range was used to generate a sagittal projection. Then the width of the sagittal projection 173–406 was taken as the slice range for the coronal projection. Then finally, the average of the sagittal and coronal bounding box height was utilized to get a slice range for the axial projection.

3.3.3 ROI Detection Model

In this study, we investigated cervical spine detection using state-of-the-art object detection models trained on the generated ROI bounding boxes. We focused on architectures designed for high inference speed, primarily the You Only Look Once (YOLO) family [60] and the Real-Time Detection Transformer (RT-DETR) [61]. The YOLO series (e.g., YOLOv5, YOLOv8, YOLOv10) has become a benchmark for real-time detection, offering strong efficiency–accuracy trade-offs and incorporating advances such as anchor-free and end-to-end NMS-free designs [62] [63]. In parallel, RT-DETR provides a transformer-based alternative, building on the DETR architecture [64] with a hybrid encoder–decoder design that directly predicts object locations and classes, and recent optimizations have made it competitive with modern YOLO variants in both speed and accuracy. By evaluating representative models from both families, our study offers a comparative analysis of leading CNN-based and transformer-based approaches for ROI detection in cervical spine CT imaging [84].

Table 1 Training parameters for ROI detection models

Training parameters	Parameter value
Batch size	8
Number of folds	5
Image size	640
Max epochs	100
Epoch stopping criteria	20
Optimizer	SGD

3.3.4 Experimental Setup for ROI Detection

We employed a consistent experimental setup to ensure uniformity and reliable performance evaluation. All neural networks are trained with identical settings on Google Colab, using an NVIDIA GeForce RTX 3090 GPU (24GB VRAM), an Intel Core i9-12900K CPU (3.20 GHz), and 32GB of RAM, running Python 3.11.9 and PyTorch 2.2. Detection models are implemented with the Ultralytics v8.2.5 library and initialized with COCO Dataset pretrained weights. Hyperparameters and training parameters are summarized in **Table 1**.

3.3.5 VOI localization from 2D ROI Prediction

The variance projection gave us the best results for the prediction of 2D cervical spine ROI as reported in the Results section. The comparative results are presented in **Section 4**. Our goal is to localize the 3D cervical spine VOI within the whole CT volume from the 2D projections. 2D cervical spine ROIs were predicted on the projection of each view using our trained model. The coordinates of the 2D ROI bounding boxes were utilized to calculate the 3D VOI bounding box for the cervical spine region within the CT. **Figure 7** demonstrates the process of VOI

construction from ROI predictions. We added 20px tolerance to each side of the predicted bounding boxes before VOI construction in order to mitigate for any underprediction. This VOI was then extracted from the full CT volume to use in the later stages. The coordinates of the VOI (h, w, d) had been calculated using the following equations:

$$h = \frac{1}{2}(c_y + s_y) \pm 2t \quad (3)$$

$$w = \frac{1}{2}(c_x + a_x) \pm 2t \quad (4)$$

$$d = \frac{1}{2}(s_x + a_y) \pm 2t \quad (5)$$

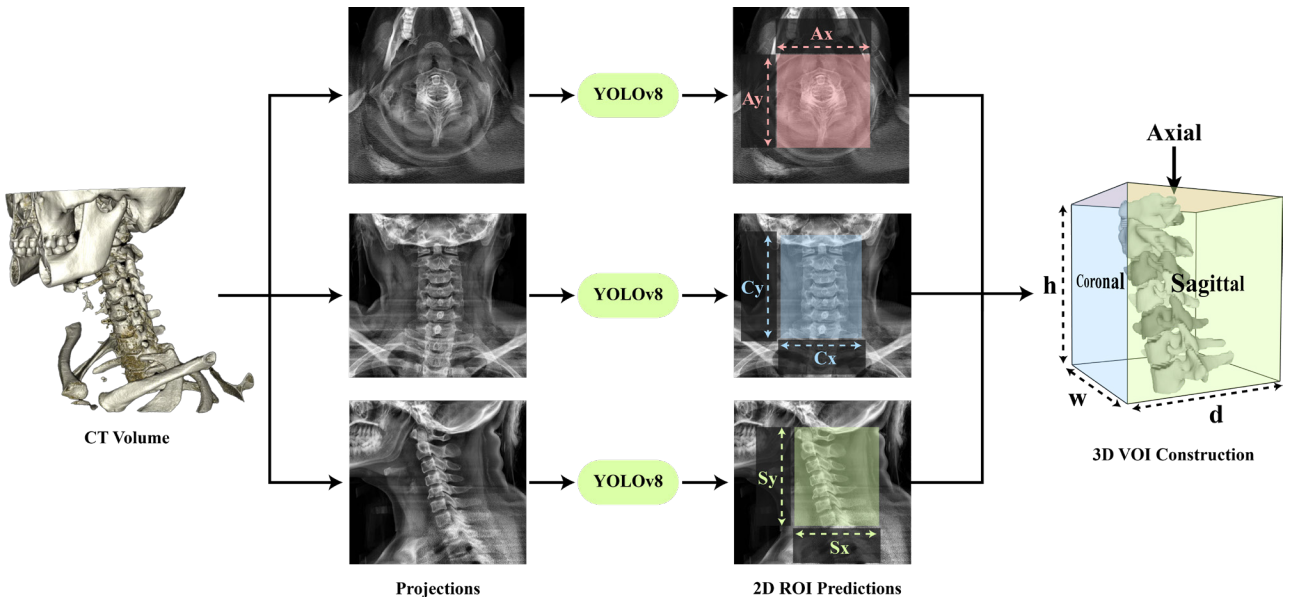


Figure 7 3D cervical spine VOI construction from 2D ROI predictions from projections

3.3.6 Evaluation Metrics

For cervical spine detection, we primarily evaluated our ROI models using Mean Intersection over Union (mIoU), a standard metric for quantifying overlap between predicted and ground truth regions in object detection and localization tasks. mIoU jointly reflects true positives, false positives, and false negatives, providing an intuitive measure of how well the predicted cervical spine VOI matches the reference annotation [65]. Given its sensitivity to both over- and under-coverage, it is well suited to assess our model's ability to accurately capture the 3D cervical spine VOI. Detailed equations for the evaluation metrics are given in the supplementary materials.

3.4. Cervical Vertebra VOI Segmentation

In this section we discuss in detail our methodology for achieving 3D segmentation from projections for the cervical spine. We utilize the ground truth that was given for 87 patients in the ground truth for training a segmentation model that can effectively segment the C1-C7 vertebrae from coronal and sagittal projections of the cervical spine. Axial projection of the whole volume was not utilized in this step as the vertebrae are not separable from a top-down view. Our goal was to approximate the location of the vertebrae, taking segmentations from two perspectives sufficed.

3.4.1 Multi-label Mask Generation

Since vertebra segmentation in this study is performed from coronal and sagittal projection images of the cervical spine VOI, anatomical overlap between neighboring vertebrae is frequently observed in these orthogonal views.

Due to cervical curvature and non-linear neck alignment in most patients, distinct vertebral structures may project onto the same spatial location in 2D, causing a single pixel in the projection image to correspond to multiple vertebrae. Further details have been provided in **Supplementary Section S4.1**.

As a result, conventional multi-class segmentation, which enforces exclusive pixel-to-class assignment, is not suitable for this task. To address this limitation, we adopt a multi-label segmentation strategy, allowing individual pixels in projection space to belong to multiple vertebral classes simultaneously. Multi-label masks are constructed by filtering the cervical vertebrae (C1–C7) from the provided 3D ground-truth segmentation and projecting each vertebra independently along the corresponding viewing axis. The resulting binary masks are then stacked into separate channels to form the final multi-label supervision.

3.4.2 Proposed Network

This study employed a modified Unet [40] architecture designed for segmenting cervical vertebrae from projection images, where the overlap of anatomical structures necessitates multi-label classification. In this approach, each pixel in the input image can belong to multiple classes simultaneously, requiring the network to generate multi-label segmentation masks. The modified Unet replaced the traditional encoder with DenseNet121 (excluding its fully connected layer) [33]. DenseNet121's dense connections and pre-trained ImageNet weights enabled the network to extract complex features and retain hierarchical representations critical for distinguishing overlapping vertebrae. Skip connections were adapted to transfer feature maps from the initial convolutional block and dense blocks of DenseNet121 to their corresponding decoder layers, ensuring that the extracted features were preserved and effectively utilized during reconstruction.

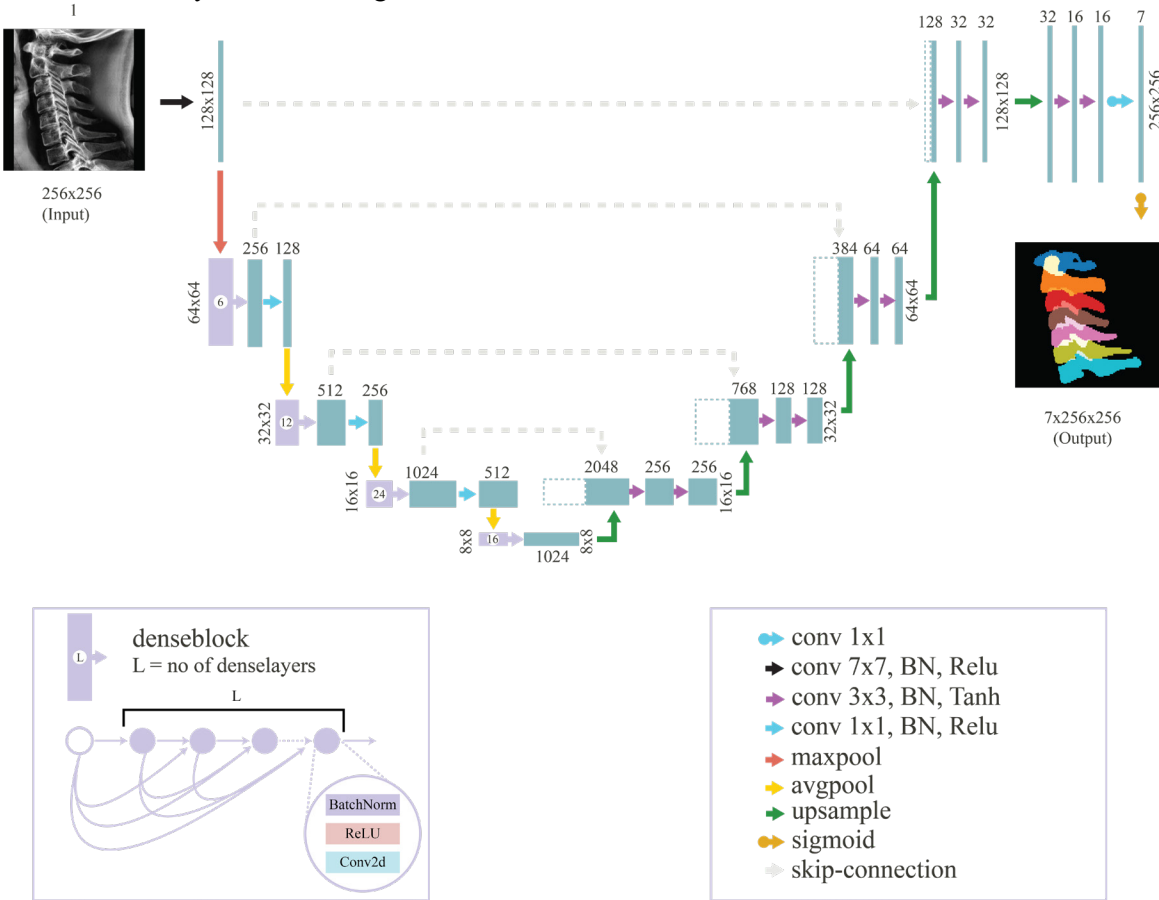


Figure 8 Proposed Segmentation Network Architecture

The multi-label capability of the network was integrated into the decoder and output layer. Instead of producing a single-channel output mask as in single-class segmentation, the decoder generated a multi-channel output, with each channel representing a probability map for a specific label. A sigmoid activation function was applied to each

channel independently, allowing the network to assign probabilities for multiple classes to each pixel. This is particularly important for cervical spine projections, where overlapping regions may belong to multiple vertebral classes simultaneously. The DenseNet121-based encoder, combined with average pooling for smoother downsampling, ensured that the model captures both global and local features necessary for precise segmentation. **Figure 8** illustrates the architecture of our proposed segmentation network.

3.4.3 Preprocessing and Data Augmentation

All projections both sagittal and coronal were square padded and resized to 256x256. 5-fold cross-validation was implemented and within each fold the train, validation and test sets had 56, 13 and 18 images respectively. The 5-fold split was kept consistent with the ROI detection stage in order to ensure there is no data leaking between steps. The train set was augmented using geometric augmentation techniques like horizontal flip and rotation. The number of images in the trainset with augmentation was 392.

3.4.4 Experimental Setup for Segmentation

The experiments for this study were conducted on the same system mentioned in the ROI detection subsection. The implementation of the DenseNet121-Unet architecture is based on the Segmentation Models PyTorch (SMP) library [66], with encoders initialized with ImageNet-trained weights [67]. To maintain consistency and ensure fair performance comparisons, all models were trained using identical settings. For efficient model convergence a learning rate scheduler was employed to drop the learning rate by a specific factor if loss didn't improve after a certain number of epochs. The complete hyperparameter configuration and training parameters are summarized in **Table 2**.

Table 2 Training parameters for segmentation models

Training parameters	Parameter value
Batch size	8
Number of folds	5
Learning rate	1e-4
Weight Decay	1e-4
Image size	256
Max epochs	120
Epoch stopping criteria	20
LR drop patience	5
Learning rate factor	0.2
Optimizer	Adam

3.4.5 Segmentation Loss Function and Evaluation Metrics

To optimize segmentation, we minimized a composite loss function that leverages the sensitivity of Dice Loss to small regions [68, 69] and the strict false-positive penalties of Jaccard Loss. The probabilistic formulations are detailed in **Supplementary Section 4.2**.

For model assessment, we evaluated spatial overlap using IoU and DSC, and boundary accuracy using the 95th percentile Hausdorff Distance (HD95) [70]. HD95 is in general preferred over standard Hausdorff distance as it excludes outliers for robust clinical relevance. To unify model ranking based on all three metrics, we utilized a normalized composite score:

$$Score = \frac{IoU}{max(IoU)} + \frac{DSC}{max(DSC)} - \frac{HD95}{max(HD95)} \quad (6)$$

3.4.6 3D Vertebra Mask Estimation and Volume Extraction

Segmentation masks were predicted for coronal and sagittal projections of 2,019 patients. To maintain anatomical fidelity, outputs were reverse-resized and unpadded to original dimensions. We approximated 3D vertebra structure by extruding and intersecting the orthogonal masks. These 3D approximations were used to crop

individual vertebrae volumes from all patient volumes. In total, 14,129 vertebrae were extracted; only ~4 were excluded due to noise-induced segmentation failure.

3.5. Cervical Vertebra Fracture Identification

Vertebra-wise fracture labels from the RSNA dataset were utilized to perform fracture classification at both the vertebra and patient levels. Following the isolation of the vertebral VOI, a neural network was trained to identify the presence of fractures within individual vertebrae. While we initially investigated 2D projection-based and full 3D volumetric approaches as baselines, our proposed 2.5D spatio-sequential framework demonstrated the most effective balance of volumetric context and diagnostic accuracy. Consequently, this section details the methodology for our proposed 2.5D approach; the comprehensive methodologies for the comparative 2D and 3D approaches are provided in **Supplementary Section S4.4**.

3.5.1 Fracture Identification using 2.5D Spatio-Sequential networks

This approach focused on leveraging spatio-sequential information within CT volumes for robust fracture classification. Unlike projection-based methods that relied on isolated 2D views, our 2.5D framework captured volumetric context by processing sequences of anatomical data. We investigated two distinct variations of this spatio-temporal approach to optimize the trade-off between contextual depth and computational efficiency. The first utilized direct volumetric slice stacks to capture immediate 3D context, while the second expanded the receptive field by employing stacks of MIPs. In both configurations, the networks predicted fracture probabilities at the sequence step level, with the final vertebra diagnosis determined via majority voting. At the patient level, we evaluated two strategies: a standard "if-any" criterion, where a patient was flagged if any vertebra was fractured, and an adaptive threshold-based method utilizing score-level fusion to maximize model agreement.

3.5.1.1 Data Preprocessing

The preprocessing pipeline for the 2.5D spatio-sequential approach was designed to overcome the limitations of single-slice analysis by incorporating volumetric context through specific stacking techniques. A bone windowing technique (width: 400 HU, level: 1400 HU) was first applied to the CT volumes to enhance the contrast of vertebral structures. To provide the network with richer spatial information, we utilized a slice-stacking strategy rather than processing isolated 2D images. For the standard approach, 15 evenly spaced slices were extracted from each vertebra VOI. Each selected slice was then augmented by stacking its two preceding and two succeeding slices along the channel axis, forming a 5-slice input stack. This configuration allowed the model to leverage local 3D spatial relationships, effectively mitigating the ambiguities often found when relying solely on individual slices.

We also investigated an alternative method aimed at expanding the anatomical context without excessively increasing the model's input dimensionality. In this variation, we extracted 75 equally spaced slices from the vertebra and formed mini-stacks of five consecutive slices (central slice ± 2). We then computed the Maximum Intensity Projection (MIP) for each mini-stack. These resulting projections were subsequently grouped into 15 sequential sets, creating stacks of projections rather than raw slices. This technique effectively increased the volumetric coverage available to the model while maintaining efficient processing dimensions. In both approaches, all input stacks were resized to $256 \times 256 \times 5$ to ensure uniformity for training. A visual example of the data is given in **Supplementary Figure S9**.

Inspired from the RSNA competition first place winner's solution [71] a variety of their data augmentation techniques were utilized to improve the model's generalizability. Initially, the images were resized to a uniform dimension. To add spatial variability, random horizontal and vertical flips, along with transpositions, were applied with a 50% chance. Adjustments to brightness and contrast further enhanced the dataset's diversity, along with transformations like shifting, scaling, and rotating. These operations, each with specific limits, helped the model adapt to minor positional variations. Beyond geometric variations, noise and blur were introduced through methods such as motion blur, median blur, gaussian blur, and gaussian noise, each with different parameters to simulate real-world image imperfections. To further prevent overfitting, CoarseDropout was implemented to randomly remove sections of the image, encouraging the model to concentrate on the more informative areas and enhancing its robustness. After these augmentations, a random permutation was applied with a 20% probability, shuffling the slice stacks within a vertebra. This creates variability in slice order, prompting the model to learn more invariant features.

Lastly, MixUp augmentation was included, where two vertebrae from the same batch are combined through a weighted random mix, producing synthetic samples to further mitigate overfitting. We evaluated our approach on 5-fold cross validation of all 2019 patients in a similar manner to previous steps. The train, validation and test splits of each fold approximately contains 9031, 2259 and 2828 vertebrae instances from 1291, 233 and 404 patients respectively.

3.5.1.2 Spatio-Sequential Fracture Identification Networks

Traditional methods that analyze individual slices independently may overlook subtle fracture patterns that span multiple slices. To overcome these limitations, we employed spatio-sequential deep learning architectures that integrate CNN-based feature extraction with sequential modeling techniques, thereby capturing both spatial and temporal dependencies. In our framework, we investigated pairing two deep learning architectures for temporal feature aggregation, LSTM [72] and Transformers [73] respectively. These networks are widely used for predicting sequential data. We implemented them after a CNN-based backbone for fracture identification from sequentially stacked slices. This architecture allowed the models to learn both local spatial features and global temporal relationships. The CNN component in both architectures extracted relevant features from each stacked set of slices, while the sequential component modeled inter-slice dependencies, effectively capturing fracture continuity across multiple slices. In our investigation CNN-Transformer outperformed CNN-LSTM networks as reported in Section 4.

Our proposed CNN-Transformer architecture, as illustrated in **Figure 9** utilized EfficientNetV2 [74] as the CNN backbone, followed by Transformer layers to model temporal dependencies. EfficientNetV2 is a highly efficient model that effectively captures spatial features from each slice in the sequence. The output from the CNN backbone is then fed into a Transformer encoder, designed to capture the sequential dependencies between slices. It employed multi-head attention mechanisms, allowing the model to focus on relevant parts of the sequence and learn the relationships between slices, which is crucial for identifying fractures that may span multiple slices. Positional Encoding was applied to the feature maps before they were processed by the Transformer so that the order of the slices is maintained and the model can grasp the sequential structure of the data. This encoding introduced information about the relative positions of each slice within the sequence. Given the sequential nature of the input, it is vital for the model to understand how each slice relates to its neighboring slices. The positional encoding enabled the Transformer to incorporate this spatio-sequential context, improving its ability to model fracture continuity across multiple slices. The Transformer encoder was made up of several layers, each containing multi-head attention followed by feed-forward networks. In our case, two Transformer encoder layers provided the best results, effectively allowing the model to capture complex relationships between slices while maintaining a tractable input dimensionality. The output from the Transformer encoder was then passed through a fully connected head that carried out the final classification or regression task, predicting the presence or absence of fractures throughout the sequence. It is important to mention that we predicted the fracture probability of each stack. For each vertebra there are 15 stacks and 15 prediction probabilities. The final vertebra-level prediction was determined from the majority vote of these 15 predictions. The model was trained end-to-end using a modified version of the Binary Cross-Entropy loss function.

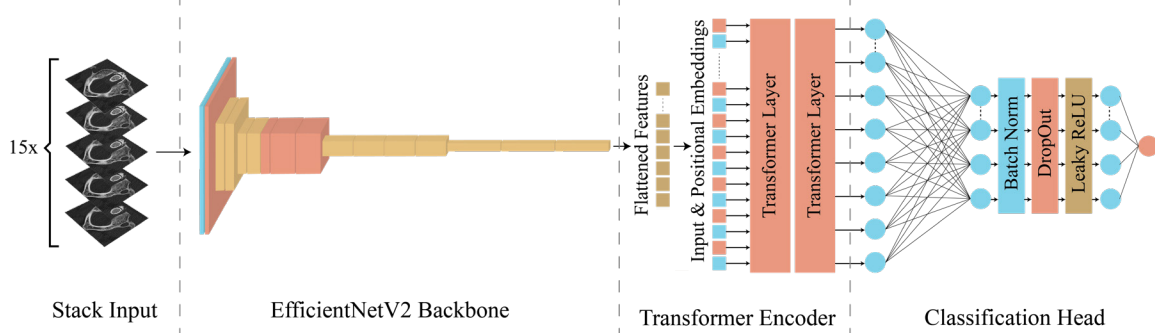


Figure 9 Proposed CNN-Transformer Architecture

3.5.1.3 Loss Function

To effectively train our binary fracture identification model, we used a modified Binary Cross-Entropy (BCE) [75] loss function that adjusted the weight of positive and negative samples to address class imbalance. In medical imaging tasks like fracture detection, the dataset is often heavily skewed, with non-fracture cases far outnumbering those with fractures. This imbalance can lead the model to favor the majority class, resulting in reduced sensitivity for detecting fractures. To tackle this problem, we have implemented a weighting mechanism in our BCE loss function that gives greater importance to fracture-positive samples, ensuring the model learns to accurately identify rare but clinically important cases.

In the standard BCE loss function, each sample contributes equally to the overall loss, meaning that positive and negative cases have the same influence on the optimization process. In our modified version, however, the loss for fracture-positive cases was scaled by a factor of two, which increases their significance during gradient updates. This approach ensures that misclassifying fractures results in a higher penalty, encouraging the model to focus on learning the features associated with fractures. The modified loss function can be expressed mathematically as follows:

$$L = -\frac{1}{\sum w_i} \sum_{i=1}^N w_i [y_i \log(\hat{y}_i) + (1 - y_i) \log(1 - \hat{y}_i)] \quad (7)$$

where w_i represented the sample weight, which was set to 2 for fracture-positive cases ($y_i = 1$) and 1 for non-fracture cases ($y_i = 0$). The denominator normalizes the total contribution to ensure stability in loss scaling. This approach allowed the network to remain sensitive to fractures without causing excessive gradient updates that could destabilize training.

3.5.1.4 Score-Fusion for enhanced vertebra-level performance

To further improve vertebra-level fracture identification, we employed a score-fusion ensembling strategy that combined the outputs of two variations of the CNN-Transformer model, one trained on a stack of normal slices and the other on a stack of MIP of stacks. While both models shared the same underlying architecture, they processed the input differently, resulting in distinct representations of vertebral structures. By averaging their output probabilities, we achieved a more robust and comprehensive fracture detection system. The key motivation behind this fusion strategy was that the two models emphasized different aspects of the vertebral anatomy. The normal stack model provided a detailed localized view, focusing on the fine-grained features present in the sampled slices, whereas the MIP of stacks model extended the coverage across a broader range of slices, capturing more global structural information. Individually, both approaches had strengths and limitations, but their combination allowed the model to benefit from both perspectives. **Figure 10** illustrates the ensemble method.

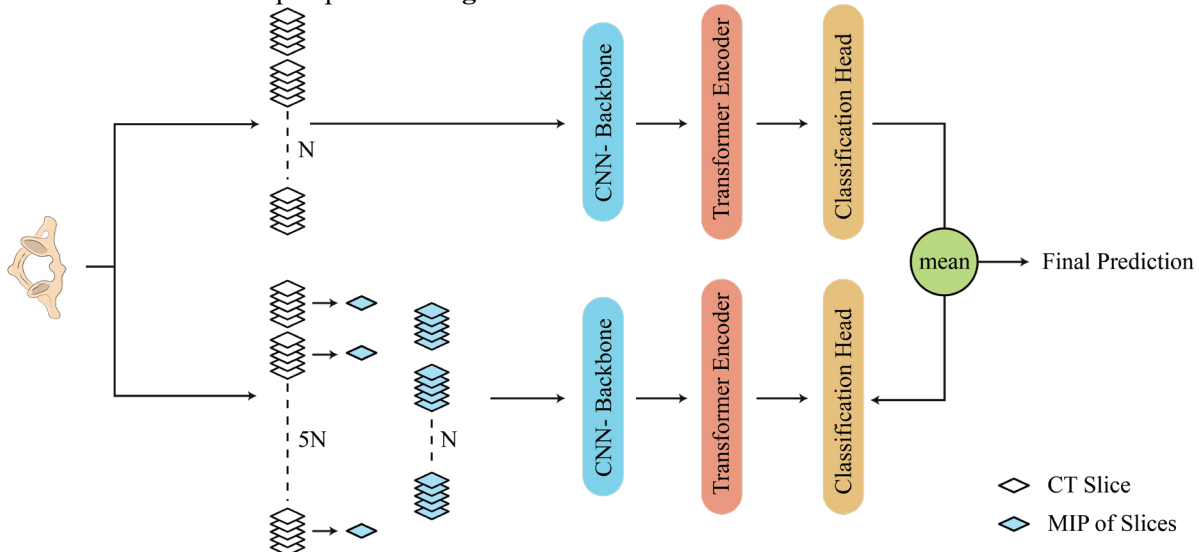


Figure 10 Proposed Ensemble Method

In our approach, we fused the probability scores of both models to derive the final classification decision. This was done by averaging or weighting the probability outputs from each model before applying the classification threshold. The intuition behind this approach was that when both models consistently predicted a fracture, confidence in the decision increased, and when they disagreed the confidence decreased. The complementary nature of their inputs allowed for a more balanced decision-making process. This fusion strategy effectively reduced false negatives by ensuring that fractures, which might have been less prominent in one representation, were still detected by the other. Our experiments demonstrated that this score-fusion ensembling significantly enhanced vertebra-level classification performance, leading to improved sensitivity and specificity. The reduction in false negatives was particularly important in medical applications where missing a fracture could have serious clinical implications.

3.5.1.5 Patient Level Fracture Prediction Using Adaptive Threshold

In order to translate vertebra-level predictions into a definitive patient-level diagnosis, we developed an aggregation strategy that used a dynamic, adaptive threshold. Rather than a simple binary rule, this method incorporated the degree of consensus between our two complementary 2.5D models (the slice-stack and projection-stack models) to enhance prediction reliability. The process began by calculating a mean fracture probability for each of the seven cervical vertebrae from the sequence of predictions generated by each of the two models. These two mean probabilities were then averaged to produce a single, unified fracture score that represented the fracture likelihood for that specific vertebra. The overall fracture signal for the patient was then determined by identifying the single highest score among these seven unified vertebral scores.

The final classification used a dynamic threshold that intelligently adapted based on the level of agreement between the two models for that patient. We quantified this consensus by measuring the difference between the models' mean predictions for each vertebra and then averaging this agreement metric across the entire cervical spine. Instead of applying a single, fixed cutoff, the system became more or less sensitive depending on the models' consensus. If the two models were in high agreement for a patient, a lower, more sensitive threshold was applied, as the joint prediction was considered highly reliable. Conversely, if the models disagreed, a higher, more conservative threshold was instituted. This required a much stronger fracture signal to make a positive classification, thereby minimizing the risk of false positives stemming from ambiguous or conflicting predictions. A patient was ultimately classified as having a fracture only if their highest vertebral fracture score exceeded this dynamically adjusted threshold.

3.5.2 Experimental Setup for Full-Volume Classification

To ensure a fair comparison, all 2D, 2.5D, and 3D models were trained using a standardized framework with targeted adaptations for each architectural paradigm. A 5-fold cross-validation strategy was employed across all experiments. Key training parameters were tailored to each approach. The CNN models for 2D and 2.5D approaches were implemented using the TIMM library and for the 3D approach a modified version of TIMM called TIMM-3D was utilized. A complete summary of the configurations for each approach is provided in **Table 3**.

Table 3 Training parameters for Fracture Classification Models

Training parameters	2D	2.5D	3D
Initial Learning Rate	1e-4	6e-5	1e-4
Early Stopping Patience	14	20	14
Weight Decay	1e-4	1e-4	1e-4
Batch Size	8	8	4
Input Size	224x224	15x256x256	64x224x224
Optimizer	Adam	AdamW	AdamW

3.5.3 Explainability for Fracture Identification

To enhance the clinical interpretability and trustworthiness of our proposed CNN-Transformer fracture identification model, we implemented a comprehensive explainability framework that provides insights into both spatial and sequential decision-making processes. [76, 77]. Our explainability approach operated on two complementary levels, spatial attention analysis and sequential relationship analysis. For spatial explainability, we employed Grad-CAM [38] to visualize which anatomical regions within individual vertebral slices contribute most significantly to fracture predictions. This technique generates heat maps that highlight the spatial locations where the CNN backbone focuses its attention during the classification process. By analyzing the final convolutional layers of our EfficientNetV2 backbone, we have traced the model's decision-making process back to specific anatomical structures within each of the 15 slices that comprise a vertebra volume. The resulting activation maps provide clinicians with visual evidence of fracture-relevant features, enabling verification of whether the model's spatial focus aligns with clinical expectations [78].

To complement spatial analysis, we extracted and visualized attention patterns from the transformer component of our architecture. The transformer's self-attention mechanism [73] naturally captures relationships between different slices within a vertebra sequence, revealing which temporal positions the model considered most informative for fracture detection. These attention patterns demonstrate how the model integrates information across the slice sequence, showing whether certain anatomical positions consistently receive higher attention or if the model dynamically adjusts focus based on vertebra-specific characteristics. The attention matrices provide insights into the sequential reasoning process, illustrating how fracture patterns spanning multiple slices contributed to the final diagnostic decision [79, 80].

3.5.3.4 Evaluation Metrics for Fracture Identification

The performance of the fracture identification model was evaluated using a suite of standard classification metrics. These included Accuracy, Precision, Sensitivity, Specificity, and the F1-Score. Additionally, the Area Under the Receiver Operating Characteristic Curve (ROC-AUC) was computed to assess the model's overall discriminative capability.

3.5.4 Interobserver Variability Test

To assess the reliability and consistency of fracture classification, we performed an interobserver variability analysis on a subset of 30 randomly sampled patients from the dataset. These cases were anonymized and independently evaluated by three expert radiologists, each of whom was provided with the same set of CT volumes under different names. This design ensured that the radiologists assessed the cases without bias and allowed us to investigate whether fractures could be consistently identified across different observers. Their annotations were then compared with the original RSNA dataset labels as well as with the predictions generated by our proposed models, enabling a comprehensive evaluation of both human and model-level consistency. The agreement was quantified using pairwise Cohen's Kappa [81] and Fleiss' Kappa [82]. Cohen's Kappa (κ) measures the agreement between two annotators while correcting for chance agreement, defined as:

$$\kappa = \frac{p_o - p_e}{1 - p_e} \quad (8)$$

Where p_o is the observed agreement and p_e is the expected agreement by chance. To extend this to multiple annotators, Fleiss' Kappa (κ_F) was used, defined as:

$$\kappa_F = \frac{\bar{P} - \bar{P}_e}{1 - \bar{P}_e} \quad (9)$$

where \bar{P} is the mean observed agreement across all subjects and \bar{P}_e is the mean expected agreement. These metrics provided a robust evaluation of labeling consistency across experts and models, offering valuable insight into the reproducibility of fracture detection and the degree to which our models aligned with radiologist-level performance.

4. Results

In this section, we discuss the results of our investigation in six subsections. The first subsection reports a comparative analysis of various object detection models used for cervical spine VOI detection. The next subsection presents a thorough evaluation of multi-label segmentation from different projections using state-of-the art segmentation models. The third subsection discusses the results of different approaches to fracture detection both in the vertebra and patient level. The fourth subsection shows a thorough ablation study of our classification model. The fifth and final subsection discusses interobserver variability by comparing the classification decision by different models with three domain experts and the annotation provided in the RSNA dataset. Finally, the last subsection compares the performance of our approach to existing approaches in the literature.

4.1 Cervical Spine VOI Detection

ROI detection of the cervical spine was evaluated using 5-fold cross-validation across 87 patients, utilizing 3D mIoU as the primary metric for localization accuracy. We assessed multiple size variants of YOLO (v5, v8, v9, v10) and RT-DETR architectures across Max, Mean, Gradient, and Variance projections.

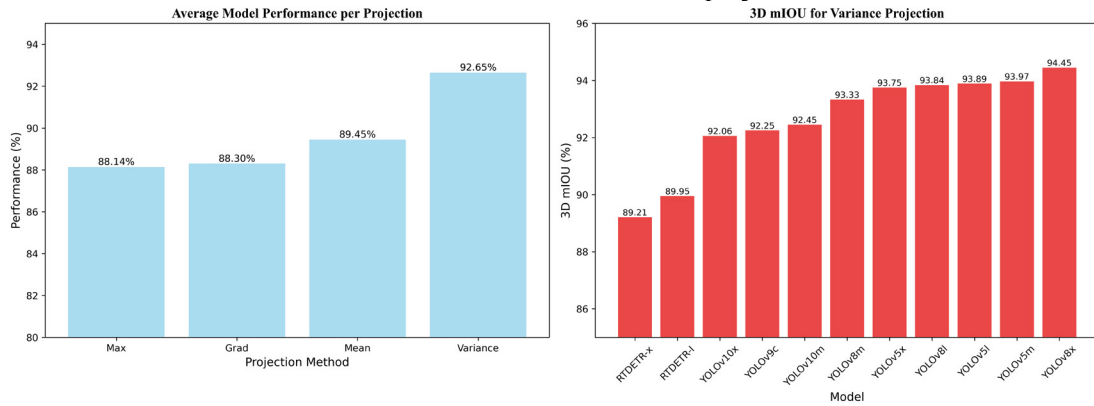


Figure 11 Comparative Performance of ROI Detection Models on Variance Projection

Among the projection strategies, variance projection proved to be the most effective. As illustrated in **Figure 11** (Left), it achieved the highest average performance across all models (92.65%) compared to Mean (89.45%), Gradient (88.30%), and Max (88.14%) projections. Variance projection effectively highlights inter-slice intensity fluctuations, providing a more stable representation of the vertebral column compared to MIP, which can obscure fine details by emphasizing high-intensity regions. Under the optimal variance setting, YOLOv8x achieved the top performance with a 3D mIoU of 94.45%, as shown in **Figure 11** (Right). Furthermore, our ablation study on preprocessing confirmed the value of volume interpolation, which increased the 3D mIoU of the YOLOv8x model from 93.46% to 94.45%. A qualitative comparison of the top-performing models has been presented in **Figure 12**, demonstrating the robustness of the v8 and v5 architectures in localizing the spine.

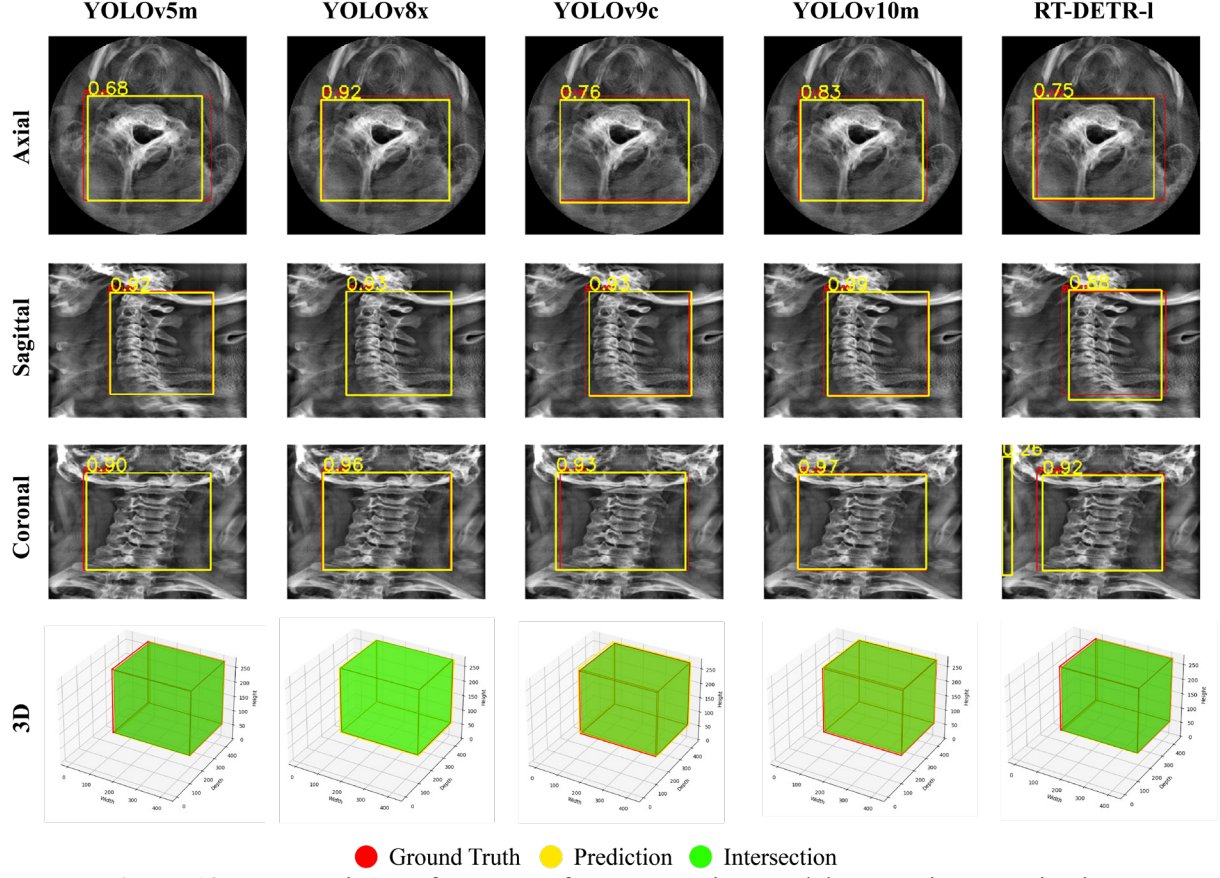


Figure 12 Comparative Performance of ROI Detection Models on Variance Projection

Based on these findings, we used the predictions from the YOLOv8x model with Variance projections to extract the cervical spine VOI from all 2019 patient scans, and used those VOIs for subsequent analysis in the following stages of the study. Detailed results for all projection types and models are provided in **Supplementary Section S5**.

4.2 Multi-label Vertebra Segmentation

This section evaluates the performance of the multi-label segmentation model, examining the choice of architecture, projection strategies, and the anatomical variation across vertebrae.

4.2.1 Comparison of Different Segmentation Models

Table 4 presents a comparative analysis of different segmentation models on both sagittal and coronal projections, along with their average performances. All model performances reported here are on the energy projection which is our overall best projection.

Table 4 Comparative Performance of Segmentation Models

Model	Sagittal			Coronal			Average			
	IoU↑	DSC↑	HD95↓	IoU↑	DSC↑	HD95↓	IoU↑	DSC↑	HD95↓	Score↑
SE_ResNext101_UperNet	74.87	85.60	4.42	77.22	87.12	4.28	76.05	86.36	4.35	1.044
EfficientNetv2_Segformer	74.06	85.05	4.55	77.84	87.52	4.09	75.95	86.29	4.32	1.048
EfficientNetv2_DeepLabV3+	73.96	85.00	4.61	77.99	87.61	4.06	75.97	86.30	4.33	1.046
DenseNet169_Unet++	73.65	84.79	4.70	77.50	87.30	4.20	75.58	86.05	4.45	1.011
EfficientNet-b2_MAnet	73.86	84.93	4.52	76.95	86.95	4.49	75.41	85.94	4.50	0.997
MobileNetv2_Linknet	73.61	84.76	4.82	77.27	87.15	4.29	75.44	85.96	4.56	0.984
MiT_b0_SegFormer	74.10	85.10	4.56	76.40	86.60	4.56	75.25	85.85	4.56	0.981

EfficientNet-b2_FPN	72.65	84.11	4.96	77.32	87.19	4.30	74.98	85.65	4.63	0.959
DenseNet121_Uenet (Proposed)	78.53	87.93	4.17	78.36	87.79	4.83	78.45	87.86	4.50	1.060

Our proposed model, DenseNet121_Uenet, demonstrated superior performance compared to other evaluated architectures. It achieved the highest average IoU of 78.45% and an average DSC of 87.86%. Furthermore, it obtained the top overall score of 1.060. In the sagittal view, the DenseNet121_Uenet achieved an IoU of 78.53%, a DSC of 87.93%, and an HD95 of 4.17 mm, outperforming all other models in this projection for IoU and Dice, and achieving the lowest (best) HD95. In the coronal view, the DenseNet121_Uenet obtained an IoU of 78.36% and a DSC of 87.79%. While its coronal HD95 of 4.83 mm was not the lowest, its IoU and DSC remained highly competitive. For instance, EfficientNetv2_DeepLabV3+ showed a slightly better HD95 (4.06 mm) in this specific view. However, the proposed model consistently showed strong and balanced performance across both views which contributed to its leading average scores. Other models like EfficientNetv2_Segformer and EfficientNetv2_DeepLabV3+ also showed strong results, achieving scores of 1.048 and 1.046, respectively, with notable performance in the coronal projection, particularly regarding HD95. Nevertheless, the DenseNet121_Uenet consistently provided high IoU and Dice values across both views, and a decent HD95 score leading to the best overall average performance. Since our main goal is to use the segmentation to crop out vertebra volumes that we are ultimately going to use for classification, small boundary inaccuracies are negligible.

4.2.2 Performance Breakdown on Individual Cervical Vertebrae

A detailed vertebra wise analysis of the proposed DenseNet121_Uenet is reported in **Table 5**. Overall, the model achieves consistently strong performance across all cervical levels, with accuracy patterns that closely follow the underlying anatomy.

Table 5 Segmentation Performance of Different Cervical Vertebra

Class	Sagittal			Coronal			Average		
	IoU↑	Dice↑	HD95↓	IoU↑	Dice↑	HD95↓	IoU↑	Dice↑	HD95↓
C1	79.23	88.19	4.08	79.70	88.60	3.63	79.46	88.39	3.86
C2	83.16	90.22	2.50	83.15	90.72	3.35	83.15	90.47	2.93
C3	77.86	87.21	3.80	75.79	85.98	5.61	76.82	86.60	4.70
C4	77.34	86.97	4.27	74.81	85.33	5.80	76.07	86.15	5.04
C5	75.42	85.75	5.33	77.13	86.96	5.03	76.28	86.35	5.18
C6	77.26	86.94	4.77	79.40	88.38	4.32	78.33	87.66	4.55
C7	79.97	88.69	4.41	79.24	88.30	6.04	79.61	88.50	5.22

The C2 vertebra (Axis) shows the best performance, with the highest average IoU and Dice and the lowest HD95 (2.93 mm). This is consistent with its distinctive dens, which provides a stable and highly discriminative landmark for the network to localize and segment. C1 (Atlas) and C7 (Vertebra Prominens) also achieve high Dice values (around 88–89 percent), likely due to their characteristic ring shaped configuration (C1) and the prominent, non-bifid spinous process of C7. Despite its good overlap, C7 presents the largest average HD95, driven mainly by the coronal view, suggesting that fine boundary delineation around its broad transverse processes and the C7–T1 junction remains challenging.

In contrast, the typical mid cervical vertebrae C3, C4, and C5 exhibit slightly lower IoU and Dice and higher HD95 compared to C1, C2, and C7. These vertebrae share more homogeneous morphology, with similar body size and bifid spinous processes, and their spinous processes are frequently obscured by the vertebral bodies in coronal projections. This combination of structural similarity and occlusion reduces the availability of distinct visual cues and explains the modest drop in performance and increased boundary ambiguity. C6 performs marginally better than C3–C5 and approaches the accuracy of C1 and C7, indicating that the model remains stable toward the lower cervical region.

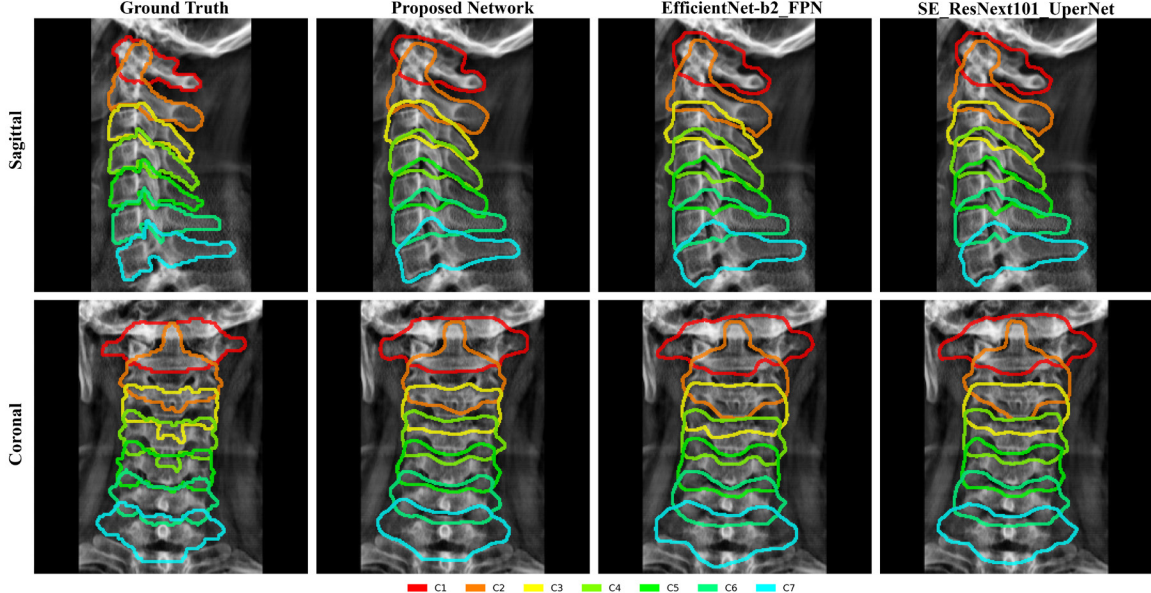


Figure 13 Side by Side Multi-label Segmentation Performance Comparison

Qualitative examples in **Figure 13** illustrate these trends. The proposed DenseNet121 Unet produces more compact and anatomically plausible masks than the comparison models, especially around overlapping vertebral structures. At the same time, all methods struggle to fully capture the spinous processes of the mid cervical vertebrae in the coronal view, consistent with the higher HD95 values reported in **Table 5**. Given that our downstream task relies on accurate vertebra centered cropping rather than exact subvoxel boundary placement, these residual boundary errors are acceptable, while the observed volumetric consistency across C1–C7 confirms the suitability of DenseNet121_Unet for multi label cervical vertebra segmentation.

4.2.3 Ablation Study for Segmentation Network

To identify the most effective 2D representation for vertebra segmentation, we evaluated 23 projection techniques with the proposed DenseNet121 Unet on both sagittal and coronal views, using five fold cross validation. The vertebra specific IoU and Dice trends are summarized in **Figure 14**, while the full quantitative results, including HD95 and the global projection scores, are reported in **Supplementary Table S4**.

In **Figure 14**, the Energy projection (red curve) consistently traces the outer envelope of the radar plots across all vertebrae from C1 to C7 for both IoU and Dice, indicating that it dominates all other projections at every cervical level. Projections such as Inversion, Standard Deviation, and Variance form inner contours that remain close to Energy, reflecting competitive but slightly lower performance. In contrast, edge based projections like Gradient, Edge, and Hessian occupy the inner region of the plots with markedly smaller radii, showing reduced accuracy across all vertebrae. These patterns confirm that projections which preserve rich intensity statistics and bone contrast (for example Energy and variance based methods) are more informative for vertebral segmentation than those that rely mainly on sparse edge responses. **Supplementary Figure S12** provides qualitative examples that mirror the radar plot, where Energy projection produces the most compact and anatomically faithful vertebral masks with fewer false positives than suboptimal projections.

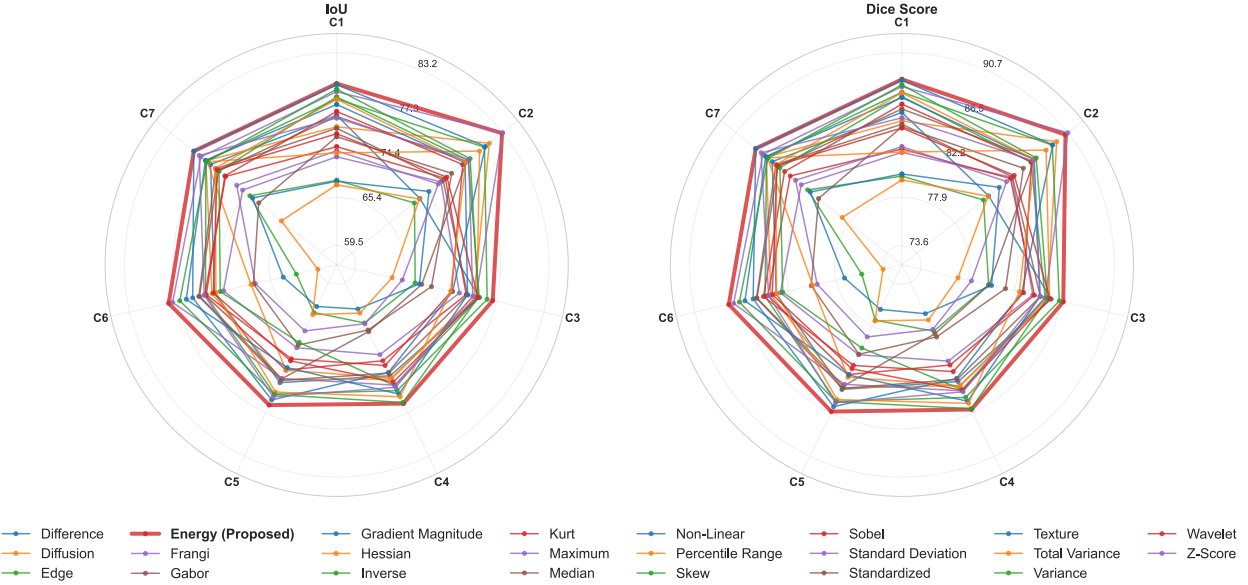


Figure 14 Vertebra-Specific IoU and Dice Score Radar Plot Across 23 Projection Techniques

Preprocessing ablations further showed that bone windowing before projection improved Dice and IoU by 1.82 and 2.60 percentage points respectively, while volume interpolation to at least 400 slices increased Dice by 5.51 points and reduced HD95 by 2.80 mm. Therefore, all subsequent experiments use Energy projection combined with bone windowing and volume interpolation as the default configuration for vertebra segmentation and downstream fracture classification. Additional supporting results are provided in **Supplementary Section S6**.

4.3 Fracture Classification

4.3.1 Fractured Vertebra Recognition

We systematically evaluated the performance of multiple classification strategies with different input modes including 2D projection-based, full-volume 3D, and 2.5D inputs on the task of identifying fractures at individual cervical vertebrae (C1–C7). All 2D models were trained and evaluated on variance projection of vertebrae in each respective orthogonal view. For 2.5D and 3D inputs, the raw slices with bone window applied were utilized unless mentioned otherwise. **Table 6** presents the aggregate classification performance across all 5 folds for these methods.

Conventional 2D approaches on the variance projection, while computationally lightweight, show substantial limitations in capturing the anatomical continuity and spatial context needed for reliable fracture detection. Axial projections performed better than sagittal and coronal views, but all single view 2D models exhibited poor sensitivity and low F1 scores. Multi-view 3-channel fusion further degraded performance relative to axial alone because the views lack spatial correspondence. The 3D EfficientNet-B0 model achieved high specificity and a strong AUC by leveraging full volumetric context but still yielded a low F1-score due to overfitting, likely driven by the complexity of the full 3D input space.

Table 6 Performance Comparison of Vertebra Fracture Recognition Networks

Input	View	Model	Accuracy	Precision	Sensitivity	Specificity	F1-Score	ROC-AUC
2D	Axial	DenseNet121	87.52	29.8	16.34	95.62	21.11	31.3
2D	Coronal	DenseNet121	13.82	10.33	96.81	4.37	18.67	43.89
2D	Sagittal	DenseNet121	50.05	12.93	67.80	48.03	21.72	50.05
2D	Fused	DenseNet121	87.2	27.64	15.58	95.36	19.93	87.2
2D	Fused	Resnet18	60.63	10.33	37.12	63.31	16.16	60.63
3D	-	EfficientNetB0	89.72	49.2	17.11	97.99	25.39	73.42
2.5D (Slice Stacks)	Axial	Proposed Network	93.55	72.16	62.31	97.09	66.54	90.19
2.5D (Max Projection Stacks)	Axial	Proposed Network	93.69	76.83	56.55	97.95	64.60	89.85
-	-	Proposed Network (Score Fusion)	94.51	84.16	57.49	98.74	68.15	91.62

In contrast, the proposed 2.5D CNN-Transformer framework achieved the most favorable overall performance. By processing either stacked axial slices or maximum-intensity projection stacks, it effectively captured both localized morphological cues and global vertebral context. Score-level fusion of these two variants further enhanced robustness, yielding an 8% increase in precision and a 2% gain in F1-score over the slice-stack model, despite a ~5% drop in sensitivity. This ensemble provided the best balance among precision, sensitivity, and specificity, outperforming all baselines.

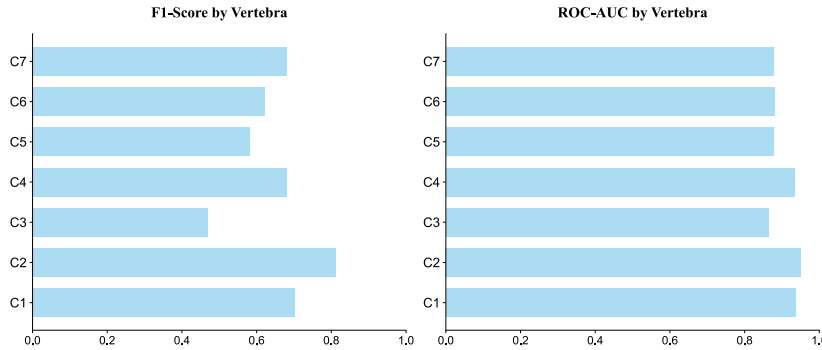


Figure 15 Vertebra-wise comparison of fracture classification performance across C1–C7 for our proposed model.

A vertebra-wise breakdown of performance, illustrated in **Figure 15**, the bar charts reveal distinct diagnostic patterns across the cervical spine. The model achieved its highest F1-scores on C2 and C1, likely benefiting from their distinct anatomical features and high fracture prevalence. Conversely, the lowest F1-score occurred at C3, which correlates with it having the lowest fracture prevalence in the dataset (see **Supplementary Figure S1** for fracture distribution). Interestingly, C4 demonstrated a sharp recovery, outperforming C6 despite having significantly fewer training examples. Performance peaked again at C7, aligning with its status as the most frequently fractured vertebra. This non-linear trend suggests that while dataset imbalance drives performance at the extremes, anatomical complexity and imaging artifacts likely constrain the mid-lower spine. Crucially, the model maintained high discriminative ability (ROC-AUC >0.85) across all vertebrae, confirming its robustness even where specific decision thresholds varied.

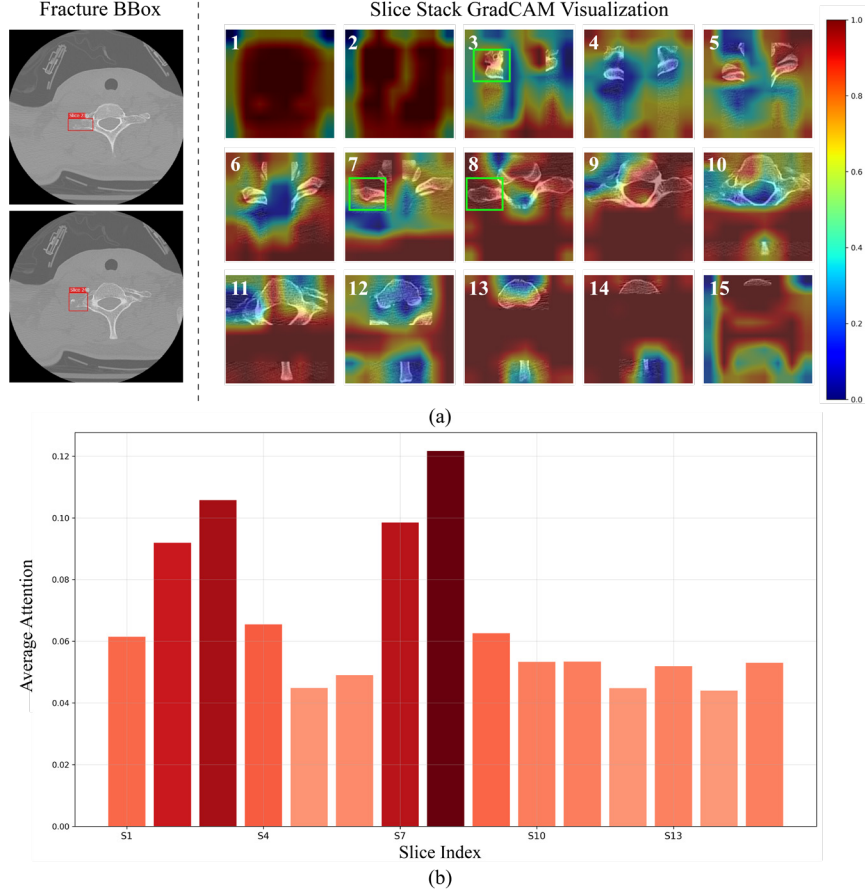


Figure 16 (a) Slice-wise GradCAM visualization (b) Average attention per slice

Figure 16 demonstrates the explainability analysis for a representative vertebra case that was correctly classified as fractured by our proposed 2.5D CNN-Transformer model. The visualization illustrates both spatial and sequential aspects of the model's decision-making process. In **Figure 16 (a)**, the Grad-CAM analysis reveals the spatial attention patterns across all 15 slice stacks, with the heat maps overlaid on the original CT slices using a color scale where red indicates regions of highest model attention. The ground truth fracture location is indicated by the bounding box annotations on the reference slices (left panel). **Figure 16(b)** presents the corresponding attention weights extracted from the transformer component, quantifying how much each slice stack contributes to the final fracture prediction. The analysis reveals that the model predominantly focuses on slice stacks 3, 7, and 8, which exhibit the top 3 highest average attention scores compared to other positions in the sequence. Notably, the spatial attention patterns in these high-weighted slices include the anatomical regions where the ground truth fracture is located (highlighted with green boxes in the visualization). This alignment between the model's spatial focus areas and the actual fracture location provides evidence that the CNN-Transformer architecture has learned clinically relevant features and demonstrates appropriate diagnostic reasoning. The convergence of high sequential attention weights with spatially accurate activation maps validates the model's ability to identify both the relevant anatomical positions within the vertebra sequence and the specific morphological patterns indicative of fracture pathology.

Taken together, these findings support the viability of the proposed projection-driven pipeline for vertebra-level fracture detection. By leveraging spatio-sequential representations, the 2.5D ensemble model enables accurate classification without requiring full-resolution 3D data.

4.3.2 Patient Level Fracture Recognition

For effective clinical decision-making, achieving a reliable patient-level diagnosis is also important. This section details our investigation into several distinct strategies to classify a patient as having a cervical fracture. We

evaluated methods ranging from direct classification on 2D projections of the entire cervical spine to more complex approaches that aggregate vertebra-specific fracture predictions into a final patient-level outcome for 3D and 2.5D approaches. The performance of the best models from each input type is presented in **Table 7**.

Table 7 Patient Level Performance Comparison of Different Models

Input	View	Model	Aggregation Method	Accuracy	Precision	Sensitivity	Specificity	F1-Score	ROC-AUC
2D (whole)	Coronal	DenseNet121	-	60.99	59.16	58.55	63.21	58.85	64.63
2D (whole)	Sagittal	DenseNet121	-	59.26	64.58	32.12	83.96	42.9	59.26
		DenseNet121 (Score Fusion)	-	66.67	66.86	59.59	73.11	63.01	69.76
2D	Axial	DenseNet121	If Any	61.42	65.64	39.75	81.1	49.51	34.04
2D	Coronal	DenseNet121	If Any	47.6	47.6	100	0	64.5	46.22
2D	Sagittal	DenseNet121	If Any	48.34	47.93	98.65	2.65	64.51	44.94
3D		EfficientNetB0	If Any	62.00	74.14	30.56	90.43	41.38	65.79
2.5D (Slice Stacks)	Axial	Proposed Network	If Any	82.67	86.15	76.18	80.50	80.66	89.09
2.5D (Max Projection Stacks)	Axial	Proposed Network	If Any	81.18	88.87	69.79	77.07	77.87	89.15
		Proposed Network (Score Fusion)	If Any	83.06	93.54	69.31	95.54	79.58	90.95
		Proposed Network (Score Fusion)	Adaptive Average	83.06	82.01	82.52	83.55	82.26	83.04

Initial investigations using 2D deep learning models on single projections of the entire cervical spine volume yielded suboptimal results. A DenseNet121 model trained on coronal projections achieved an F1-score of only 58.85%, and the performance on sagittal projections was even lower, with an F1-score of 42.9%. A score-level fusion of these two views provided only a marginal improvement, reaching an F1-score of 63.01%. These findings suggest a fundamental limitation of whole-volume projection methods. The compression of 3D anatomical data into a single 2D lateral view obscures fine-grained details and localized fracture patterns, thus hindering the model's diagnostic accuracy.

A more intuitive approach involves aggregating the predictions from individual vertebra models. We first tested a simple "If Any" decision rule, where a patient is classified as positive for fracture if any of their seven cervical vertebrae are predicted as fractured. When applied to the 2D projection-based vertebra classifiers, this method proved highly unreliable. While the axial-view model produced a modest F1-score of 49.51%, the models for the coronal and sagittal views demonstrated extreme class polarization, achieving near-perfect sensitivity at the cost of nearly zero specificity. This is obvious as the underlying 2D vertebra classifiers were not robust enough, leading to excessive false positives and rendering the simple aggregation method clinically unviable. Also, the same approach applied to 3D model resulted in a sub-optimal F1-score of 41.38%. In sharp contrast, applying the "If Any" rule to our proposed 2.5D spatio-sequential models yielded a significant leap in performance as the classifiers were already performing effectively for the vertebra level classification. The model trained on axial slice stacks achieved a patient-level F1-score of 80.66% and a ROC-AUC of 89.09%. Fusing the outputs of the slice-stack and max projection-stack models further refined performance, reaching an impressive precision of 93.54% and specificity of 95.54%. However, this high precision came with a notable trade-off as the sensitivity dropped to 69.31%. While minimizing false positives is important, such a reduction in sensitivity is a critical drawback in a diagnostic setting, as it increases the risk of missing true fractures. To address this limitation and achieve a more clinically relevant balance, we utilized an adaptive average fusion strategy. This approach produced the most well-rounded and superior results, achieving a patient-level F1-score of 82.26%, with a precision of 82.01%, specificity of 83.55%,

and a high sensitivity of 82.52%. Given that the dataset is well-balanced at the patient level, with 961 fractured cases out of 2,019 total patients, the model's high accuracy of 83.06% is also a meaningful indicator of its robust overall performance. By successfully retaining high sensitivity while also maintaining strong precision, the adaptive method proves far more robust and clinically reliable than the simpler "If Any" rule.

4.3.3 Ablation Study for Classification Network

To optimize the architecture, we conducted ablation studies on the sequential modeling component and regularization strategies. As summarized in **Table 8**, the CNN-Transformer with 2 encoder layers demonstrated superior performance compared to the LSTM baseline and other transformer depths, achieving the highest F1-score (66.54%) and ROC-AUC (90.19%). While increasing depth to 3 layers led to overfitting, the 2-layer configuration provided the optimal balance of discriminative power and stability. Additionally, we investigated the impact of Mixup augmentation, finding that it significantly improved model generalization by boosting the F1-score from 61.61% to 66.54% and ROC-AUC from 88.33% to 90.19% (see **Supplementary Figure S7** for full details).

Table 8 Ablation Study on the Sequential Modeling Component.

Sequential Component	Number of Layers	Accuracy	Precision	Sensitivity	Specificity	F1-Score	ROC-AUC
LSTM	2	93.70	75.36	58.67	97.73	65.67	89.83
Transformer	1	93.11	68.92	60.35	96.85	64.00	89.12
Transformer	2	93.54	72.16	62.31	97.09	66.54	90.19
Transformer	3	93.22	71.37	58.86	97.17	63.90	88.95

4.3.4 Interobserver Variability Analysis

This section details our analysis on interobserver variability among expert radiologists and our model. We separately evaluated the experts against each other and against our model and the dataset's ground truth.

4.3.4.1 Inter-Rater Agreement Among Experts

The analysis of consensus among the four raters, including three radiologists and the Ground Truth (GT), revealed a moderate but imperfect level of agreement, underscoring the subjective nature of fracture interpretation. As illustrated in **Figure 17**, the overall agreement at the patient level was moderate, with a Fleiss' Kappa (κF) of 0.669, and a similar level of consensus was found when considering all vertebrae collectively ($\kappa F = 0.626$). The vertebra-specific analysis exposed significant disparities in diagnostic consistency across the cervical spine. The highest consensus was observed for the C2 vertebra ($\kappa F = 0.746$), which approaches a substantial level of agreement, likely attributable to its distinct anatomical landmarks, such as the dens, which make fractures more consistently identifiable. The C1, C6, and C7 vertebrae also showed moderate agreement, with κF values of 0.643, 0.643, and 0.630, respectively. Strikingly, agreement plummeted for the mid-cervical vertebrae. C4 showed only fair agreement ($\kappa F = 0.310$), while C3 and C5 yielded kappa scores of -0.011, indicating a complete lack of agreement beyond chance. This highlights that certain anatomical regions are exceptionally challenging to assess, leading to significant divergence in expert opinion. But this is also partly due to the small number of fractures present in these vertebrae in the chosen subset.

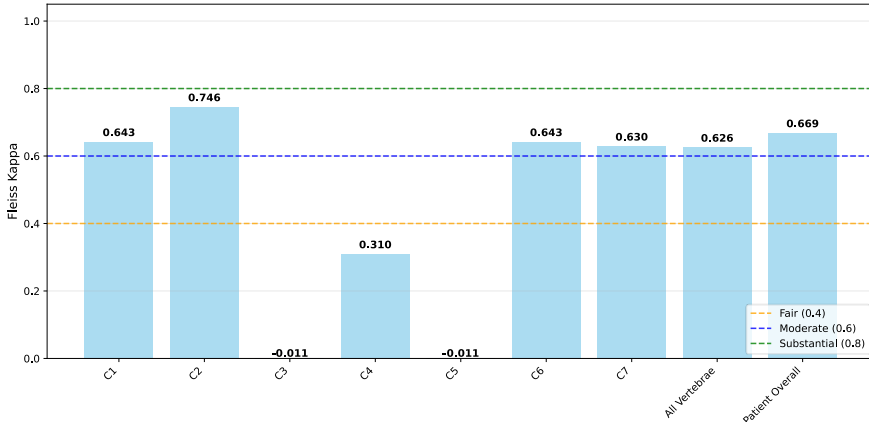


Figure 17 Interobserver Variability Among the 3 radiologists and the dataset ground truth.

To further dissect the sources of this variability, we analyzed pairwise agreement using Cohen's Kappa, as shown in the heatmaps in **Figure 18**. This analysis revealed a consistent and insightful pattern that the radiologists often had higher agreement with each other than with the ground truth, and there were clear differences in individual diagnostic patterns. At the patient level, Radiologist 1 demonstrated the highest concordance with the ground truth, achieving a moderate agreement ($\kappa = 0.67$). In contrast, Radiologist 3 showed the lowest agreement with the ground truth, with a kappa score of 0.40, indicating only fair agreement. The inter-radiologist relationships were also insightful. The agreement between Radiologist 1 and 2 was substantial ($\kappa = 0.80$), as was the agreement between Radiologist 2 and 3 ($\kappa = 0.70$). However, the agreement between Radiologist 1 and 3 was weaker ($\kappa = 0.52$), suggesting that Radiologist 3 was a relative outlier in the group, diverging more significantly from the diagnostic pattern of Radiologist 1.

This trend became even more pronounced at the more challenging vertebra level (see **Supplementary Figure S13**). Here, the agreement with the ground truth dropped for all experts, reinforcing the difficulty of the task. Radiologist 2 had the highest agreement with the GT at this granular level, though it was still only fair ($\kappa = 0.46$). Radiologist 1 showed the lowest agreement with the GT ($\kappa = 0.37$). The inter-radiologist agreement pattern again highlighted Radiologist 3 as having a distinct interpretive style, showing only moderate agreement with Radiologist 1 ($\kappa = 0.51$) and Radiologist 2 ($\kappa = 0.59$). Meanwhile, the substantial agreement between Radiologist 1 and 2 persisted ($\kappa = 0.76$). This consistent pattern across both patient and vertebra levels strongly suggests not only a systematic difference between the collective expert interpretation and the dataset's reference standard but also significant individual variations in diagnostic criteria among clinicians.

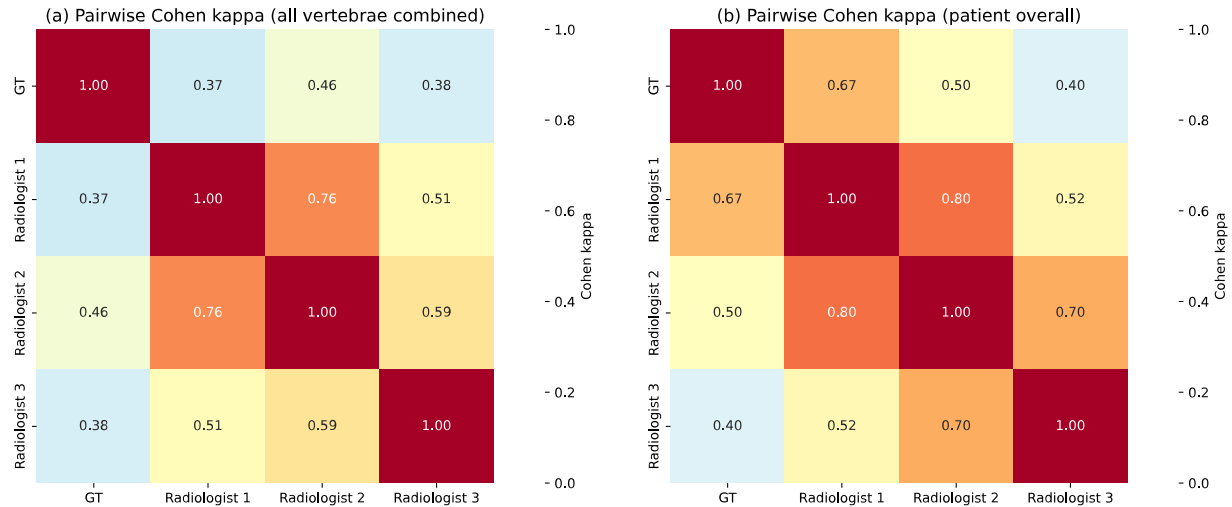


Figure 18 Pairwise Cohen Kappa Scores Among Radiologists and Ground Truth

4.3.4.2 Model Performance vs. Expert Consensus

To benchmark diagnostic accuracy, we evaluated the model directly against the ground truth (GT) alongside the three radiologists. As summarized in **Figure 19**, the model demonstrated superior consistency at the granular vertebra level, achieving substantial agreement with the GT ($\kappa = 0.711$). This significantly outperformed the human experts, whose agreement ranged from 0.371 to 0.463. Furthermore, the model exhibited higher sensitivity, identifying 19 of the 29 fractures in the subset compared to a maximum of 11 identified by the radiologists (see **Supplementary Figure S14** for detailed confusion matrices).

At the patient level, the model remained highly competitive ($\kappa = 0.600$), performing comparably to the most experienced radiologist ($\kappa = 0.672$) and surpassing the others. (see **Supplementary Figure S15** for detailed confusion matrices) This analysis confirms that the proposed model offers a highly reliable, consistent second opinion, capable of reducing the diagnostic variability inherent in human interpretation.

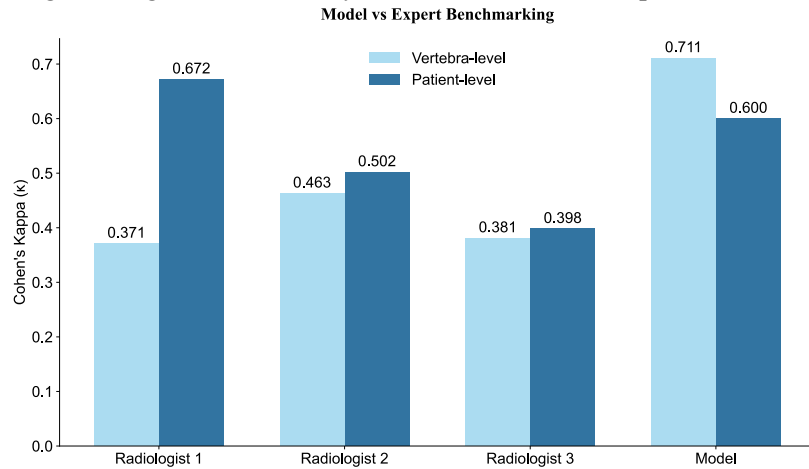


Figure 19 Comparison of Cohen's Kappa scores between the Model and Radiologists against Ground Truth

4.3.5 Comparison with State of the Art

To holistically evaluate our proposed pipeline, we situate its performance within the broader context of contemporary research, as summarized in **Table 9**. A critical review of existing literature reveals a significant challenge in direct comparisons due to methodological inconsistencies, particularly concerning the datasets used for evaluation. A number of studies have relied on small, private datasets, which may not capture the full spectrum of anatomical and pathological variability. Others have approached larger public datasets by creating artificially

balanced subsets for training and testing. While this strategy can simplify model training, it fundamentally limits the evaluation of a model's clinical utility, as real-world diagnostic scenarios are characterized by a naturally low prevalence of fractures and, thus, significant class imbalance.

Table 9 Fracture Recognition Performance Comparison with Existing Literature

Study	Dataset	Vertebra Level Results	Patient Level Results	Major Drawback
Bhavya et al. [3]	Test Set: 14 Patients	-	Accuracy: 83%	Very small test set
Nicolaes et al. [26]	Private Dataset 90 Patients Test set: 90 Patients (Cross Validation)	ROC-AUC 93%	ROC-AUC 95%	Dataset was small
Rasul et al. [29]	Subset of RSNA Dataset (4200 images) Test Set: 400 Images	Accuracy 99.75	-	Dataset was balanced before splitting.
Mahajan et al. [30]	Full RSNA Dataset	-	Accuracy 76%	-
Chlad et al. [35]	Subset of RSNA Dataset Test set size: 4330 slices	ROI mAP: 98% Fracture accuracy: 98%	-	Dataset was balanced before splitting.
Yaseen et al. [39]	Subset of RSNA Dataset 14434 slices Test set: 2887 slices	Accuracy: 97.8% F1 Score: 97.8%	-	Dataset was balanced before splitting.
Golla et al. [20]	Private dataset (355 patients) Test Set: 127 Patients	Sensitivity: 87%	-	Dataset was small
Sutradhar et al. [18]	Subset of RSNA Dataset (235 Patients) Test set: 24 Patients	mAP 93%	-	Dataset was small
Tomita et al. [41]	Private Dataset of 1432 Patients Test set: 129 Patients	-	Accuracy 89.2% F1 Score 90.8%	-
Salehinejad et al. [42]	Private Dataset of 3666 Patients Test set: 208 Patients	-	Accuracy: 70.92%	-
Kim et al. [43]	Full RSNA Dataset Test set: 404 Patients	Accuracy: 94.9%	-	-
RSNA First Place Winner	Full RSNA Dataset Test set: 2019 Patients (Cross Validation)	Accuracy: 94.05% F1-Score: 69.74%	Accuracy: 84.39% F1-Score: 82.56%	-
Proposed Method	Dataset Test set: 2019 Patients (Cross Validation)	Accuracy: 93.54% F1-Score: 66.54%	Accuracy: 82.67% F1-Score: 80.66%	
Proposed Method (Score Fusion)	Dataset Test set: 2019	Accuracy: 94.51% F1-Score: 68.15%	Accuracy: 83.06% F1-Score: 82.26%	-

Given these limitations, the most rigorous and meaningful benchmarks are those derived from studies that engaged with the full, imbalanced RSNA 2022 Cervical Spine Fracture dataset. Among these, the first-place solution from the RSNA challenge provides a strong state-of-the-art reference. Their method employed a fully 3D pipeline, using a 3D ResNet18d-Unet for voxel-level segmentation followed by a CNN-LSTM classifier, and their final submission consisted of an ensemble of nearly 20 models optimized for competitive performance. For a fair and practical comparison, we reproduced their publicly released single-model implementation based on the provided code.

Our work introduces a more computationally feasible localization paradigm by approximating 3D anatomical structures from optimized 2D projections, a method inherently more lossy than direct 3D segmentation. Despite this fundamental trade-off, our results are remarkably competitive with the state-of-the-art RSNA winner. Our ensemble model achieved a vertebra-level F1-score of 66.54% and 93.54% accuracy, closely rivaling the winner's single-model scores of 69.74% and 94.05%. This high performance was maintained at the patient level, where our model's 80.66% F1-score nearly matched the winner's 82.56%. Furthermore, when using a two-model score fusion, our performance is effectively on par (within 1%) with the RSNA winner, recording F1-scores of 68.15% at the vertebra level and 82.26% at the patient level. This close alignment in performance is a key finding of our study, demonstrating that direct 3D segmentation or slice-by-slice 2D segmentation is not an absolute prerequisite for achieving high diagnostic accuracy. Our approach affirms that approximating 3D vertebrae volumes from 2D projections is a highly viable strategy for complex fracture recognition tasks.

5. Limitations and Future Scopes

Despite the promising results of our projection-based cervical spine fracture detection pipeline, several limitations must be acknowledged regarding its clinical applicability and generalizability. Our study is primarily constrained by the characteristics of the RSNA 2022 Cervical Spine Fracture dataset, which includes strict inclusion criteria such as axial non-contrast CT scans with 1mm slice thickness, potentially limiting generalizability to diverse clinical settings with varying imaging protocols. The dataset's exclusion of post-surgical cases due to streak artifacts and altered anatomy also represents a significant limitation, as post-operative monitoring is a substantial part of clinical imaging. Furthermore, the dataset's treatment of acute and chronic fractures as equivalent entities may not reflect clinical reality where differentiation is crucial for treatment decisions.

Another primary limitation stems from the information loss associated with approximating 3D volumes from 2D projections. While this segmentation approach offers computational benefits, it can obscure subtle fracture patterns that are only visible with full volumetric context. This challenge is particularly evident with the C1 (atlas) and C2 (axis) vertebrae, where their anatomical structures can overlap in projections, potentially confounding their distinct features. Furthermore, our model's reliance on 15 equally spaced slices may be suboptimal; since fracture information is not uniformly distributed, this rigid sampling strategy might not fully capture patient-specific anatomical diversity or varying injury severity. On a functional level, our pipeline identifies which vertebrae are fractured but does not localize the exact fracture site within the bone. Finally, from an implementation standpoint, the multi-stage design creates a risk of error propagation, a sensitivity heightened by the limited ground truth data available for only 87 patients. Moreover, the computational efficiency gained from our core projection method is partially offset by the computational overhead introduced by our necessary score-fusion and transformer-based models.

We aim to overcome these limitations and further enhance the clinical utility and robustness of our approach in the future. We will explore the combination of multiple projection techniques as input to improve information retention from the 3D CT volumes. To address the scarcity of ground truth masks for segmentation, we plan to leverage self-supervised pre-training methods or pre-training on other datasets, thereby improving segmentation accuracy and generalizability. We will also investigate a computational method to precisely separate the anatomical information of the C2 (axis) from the C1 (atlas) vertebra within the extracted volumes, preventing information blending. Further investigation into a wider range of projections for fracture recognition, beyond the current scope,

and a more in-depth investigation on efficient fracture recognition networks will be conducted to both improve accuracy and efficiency of the system. Also, to enable more precise localization of fractures within an identified fractured vertebra, we will utilize localized fracture bounding box predictions. Finally, we will implement strategies to address class imbalance at the vertebra level, particularly for the mid-cervical vertebrae (C3-C5), to improve their individual fracture classification scores and overall model performance.

6. Conclusion

Our study investigated the viability of a novel pipeline for automated cervical spine fracture detection, leveraging 2D projection-based techniques to estimate 3D volumetric fracture analysis. Our three-stage pipeline has demonstrated strong performance for cervical spine localization and approximating 3D vertebral masks from 2D views. The ensemble 2.5D Spatio-Sequential model significantly enhanced fracture classification, outperforming conventional 2D and 3D approaches. Our comprehensive analysis confirmed the importance of task-specific projection selection, with variance projections excelling for localization and energy projections for segmentation which is similar to variance projection visually but finer in detail. The innovative score-fusion ensemble and advanced data augmentation techniques effectively addressed class imbalance, ensuring a robust and clinically relevant balance between sensitivity and specificity.

Furthermore, the interobserver variability analysis provides compelling evidence of our model's clinical reliability. Our model demonstrated competitive performance with the expert radiologists at both vertebra and patient levels. The results confirm that approximating 3D vertebral masks via 2D projections is an alternative to full volumetric segmentation, effectively reducing preprocessing overhead while preserving the anatomical context required for accurate fracture diagnosis. This projection-driven approach represents a significant advancement, with potential implications for revolutionizing automated diagnostic approaches in other orthopedic imaging applications and ultimately enhancing patient outcomes in cervical spine trauma management.

References

- [1] P. Copley, V. Tilliridou, and A. Jamjoom, "Traumatic cervical spine fractures in the adult," *British Journal of Hospital Medicine*, vol. 77, no. 9, pp. 530-535, 2016.
- [2] D. A. Neumann, *Kinesiology of the Musculoskeletal System-E-Book: Kinesiology of the Musculoskeletal System-E-Book*. Elsevier Health Sciences, 2016.
- [3] M. B. S. Bhavya, M. V. Pujitha, and G. L. Supraja, "Cervical spine fracture detection using pytorch," in *2022 IEEE 2nd International Conference on Mobile Networks and Wireless Communications (ICMNWC)*, 2022: IEEE, pp. 1-7.
- [4] D. Gaikwad, A. Sejal, S. Bagade, N. Ghodekar, and S. Labade, "Identification of cervical spine fracture using deep learning," *Australian Journal of Multi-Disciplinary Engineering*, pp. 1-9, 2024.
- [5] K. Inaba *et al.*, "Cervical spinal clearance: a prospective Western Trauma Association multi-institutional trial," *Journal of Trauma and Acute Care Surgery*, vol. 81, no. 6, pp. 1122-1130, 2016.
- [6] C. Zanza *et al.*, "Cervical spine injury: Clinical and medico-legal overview," *La radiologia medica*, vol. 128, no. 1, pp. 103-112, 2023.
- [7] P. M. Poonnoose, G. Ravichandran, and M. R. McClelland, "Missed and mismanaged injuries of the spinal cord," *Journal of Trauma and Acute Care Surgery*, vol. 53, no. 2, pp. 314-320, 2002.
- [8] R. Izzo, T. Popolizio, R. F. Balzano, A. M. Pennelli, A. Simeone, and M. Muto, "Imaging of cervical spine traumas," *European journal of radiology*, vol. 117, pp. 75-88, 2019.
- [9] S. Khanpara, D. Ruiz-Pardo, S. C. Spence, O. C. West, and R. Riascos, "Incidence of cervical spine fractures on CT: a study in a large level I trauma center," *Emergency radiology*, vol. 27, pp. 1-8, 2020.
- [10] A. F. Joaquim and A. A. Patel, "Thoracolumbar spine trauma: Evaluation and surgical decision-making," *Journal of craniovertebral junction and spine*, vol. 4, no. 1, pp. 3-9, 2013.
- [11] T. Sundstrøm, H. Asbjørnsen, S. Habiba, G. A. Sunde, and K. Wester, "Prehospital use of cervical collars in trauma patients: a critical review," *Journal of neurotrauma*, vol. 31, no. 6, pp. 531-540, 2014.
- [12] J. F. Holmes and R. Akkinepalli, "Computed tomography versus plain radiography to screen for cervical spine injury: a meta-analysis," *Journal of Trauma and Acute Care Surgery*, vol. 58, no. 5, pp. 902-905, 2005.

- [13] S. E. Mirvis, "Increasing workloads in radiology: Does it matter?," *Applied Radiology*, vol. 42, no. 5, pp. 6-8, 2013.
- [14] E. A. Krupinski, K. S. Berbaum, R. T. Caldwell, K. M. Schartz, and J. Kim, "Long radiology workdays reduce detection and accommodation accuracy," *Journal of the American College of Radiology*, vol. 7, no. 9, pp. 698-704, 2010.
- [15] D. Mendoza and F. J. Bertino, "Why radiology residents experience burnout and how to fix it," *Academic radiology*, vol. 26, no. 4, pp. 555-558, 2019.
- [16] S. Jalal, W. Parker, D. Ferguson, and S. Nicolaou, "Exploring the role of artificial intelligence in an emergency and trauma radiology department," *Canadian Association of Radiologists Journal*, vol. 72, no. 1, pp. 167-174, 2021.
- [17] P. Schwarzenberg, S. Darwiche, R. S. Yoon, and H. L. Dailey, "Imaging modalities to assess fracture healing," *Current osteoporosis reports*, vol. 18, pp. 169-179, 2020.
- [18] D. Sutradhar, N. M. Fahad, M. A. K. Raiaan, M. Jonkman, and S. Azam, "Cervical spine fracture detection utilizing YOLOv8 and deep attention-based vertebrae classification ensuring XAI," *Biomedical Signal Processing and Control*, vol. 101, p. 107228, 2025.
- [19] L. Q. Hung, T. D. Tuan, N. T. Hieu, and P. D. Hung, "Cervical spine fracture detection via computed tomography scan," in *Asian Conference on Intelligent Information and Database Systems*, 2023: Springer, pp. 465-474.
- [20] A.-K. Golla *et al.*, "Cervical spine fracture detection in computed tomography using convolutional neural networks," *Physics in Medicine & Biology*, vol. 68, no. 11, p. 115010, 2023.
- [21] G. R. Lee *et al.*, "Performance of the winning algorithms of the RSNA 2022 cervical spine fracture detection challenge," *Radiology: Artificial Intelligence*, vol. 6, no. 1, p. e230256, 2024.
- [22] R. Perotte *et al.*, "Improving emergency department flow: reducing turnaround time for emergent CT scans," in *AMIA Annual Symposium Proceedings*, 2018, vol. 2018, p. 897.
- [23] G. C. Jocher, Ayush; Qiu, Jing. "Ultralytics YOLOv8." <https://docs.ultralytics.com/models/yolov8> (accessed 2 March 2025).
- [24] J. Small, P. Osler, A. Paul, and M. Kunst, "CT cervical spine fracture detection using a convolutional neural network," *American Journal of Neuroradiology*, vol. 42, no. 7, pp. 1341-1347, 2021.
- [25] P. R. Esfahani *et al.*, "Development of a Machine Learning-Based Model for Accurate Detection and Classification of Cervical Spine Fractures Using CT Imaging," *Cureus*, vol. 15, no. 10, 2023.
- [26] J. Nicolaes *et al.*, "Detection of vertebral fractures in CT using 3D convolutional neural networks," in *Computational Methods and Clinical Applications for Spine Imaging: 6th International Workshop and Challenge, CSI 2019, Shenzhen, China, October 17, 2019, Proceedings* 6, 2020: Springer, pp. 3-14.
- [27] M. Sandler, A. Howard, M. Zhu, A. Zhmoginov, and L.-C. Chen, "MobileNetv2: Inverted residuals and linear bottlenecks," in *Proceedings of the IEEE conference on computer vision and pattern recognition*, 2018, pp. 4510-4520.
- [28] H. M. Lin *et al.*, "The RSNA cervical spine fracture CT dataset," *Radiology: Artificial Intelligence*, vol. 5, no. 5, p. e230034, 2023.
- [29] R. A. Rasul, P. Saha, D. Bala, S. R. U. Karim, M. I. Abdullah, and B. Saha, "Healthcare Analytics."
- [30] O. Mahajan, D. Puvathingal, Y. Kaka, A. Mangnani, and S. Suralkar, "Feasibility of Cervical Spine Fracture Detection Using Non-Conventional Slices," in *2023 2nd International Conference on Futuristic Technologies (INCOFT)*, 2023: IEEE, pp. 1-5.
- [31] J. Chen *et al.*, "Deep learning model for automated detection of fresh and old vertebral fractures on thoracolumbar CT," *European Spine Journal*, pp. 1-10, 2024.
- [32] G. Jocher. "YOLOv5 by Ultralytics." <https://github.com/ultralytics/yolov5> (accessed 2nd March 2025).
- [33] G. Huang, Z. Liu, L. Van Der Maaten, and K. Q. Weinberger, "Densely connected convolutional networks," in *Proceedings of the IEEE conference on computer vision and pattern recognition*, 2017, pp. 4700-4708.
- [34] A. Dosovitskiy *et al.*, "An image is worth 16x16 words: Transformers for image recognition at scale," *arXiv preprint arXiv:2010.11929*, 2020.
- [35] P. Chład and M. R. Ogiela, "Deep learning and cloud-based computation for cervical spine fracture detection system," *Electronics*, vol. 12, no. 9, p. 2056, 2023.

- [36] R. B. Nejad, A. H. Komijani, and E. Najafi, "Intelligent Cervical Spine Fracture Detection Using Deep Learning Methods," *arXiv preprint arXiv:2311.05708*, 2023.
- [37] A. Boonrod, A. Boonrod, A. Meethawolgul, and P. Twinprai, "Diagnostic accuracy of deep learning for evaluation of C-spine injury from lateral neck radiographs," *Heliyon*, vol. 8, no. 8, 2022.
- [38] R. R. Selvaraju, M. Cogswell, A. Das, R. Vedantam, D. Parikh, and D. Batra, "Grad-cam: Visual explanations from deep networks via gradient-based localization," in *Proceedings of the IEEE international conference on computer vision*, 2017, pp. 618-626.
- [39] M. Yaseen, M. Ali, S. Ali, A. Hussain, M. Joo, and H.-C. Kim, "Cervical Spine Fracture Detection and Classification Using Two-Stage Deep Learning Methodology," *IEEE Access*, 2024.
- [40] O. Ronneberger, P. Fischer, and T. Brox, "U-net: Convolutional networks for biomedical image segmentation," in *Medical image computing and computer-assisted intervention–MICCAI 2015: 18th international conference, Munich, Germany, October 5-9, 2015, proceedings, part III* 18, 2015: Springer, pp. 234-241.
- [41] N. Tomita, Y. Y. Cheung, and S. Hassanpour, "Deep neural networks for automatic detection of osteoporotic vertebral fractures on CT scans," *Computers in biology and medicine*, vol. 98, pp. 8-15, 2018.
- [42] H. Salehinejad *et al.*, "Deep sequential learning for cervical spine fracture detection on computed tomography imaging," in *2021 IEEE 18th international symposium on biomedical imaging (ISBI)*, 2021: IEEE, pp. 1911-1914.
- [43] D. Kim *et al.*, "Cervical Spine Fracture Detection Through Two-Stage Approach of Mask Segmentation and Windowing Based on Convolutional Neural Network," in *2023 International Conference on Platform Technology and Service (PlatCon)*, 2023: IEEE, pp. 1-6.
- [44] N. Lessmann, B. Van Ginneken, P. A. De Jong, and I. Işgum, "Iterative fully convolutional neural networks for automatic vertebra segmentation and identification," *Medical image analysis*, vol. 53, pp. 142-155, 2019.
- [45] A. Sekuboyina *et al.*, "VerSe: A Vertebrae labelling and segmentation benchmark for multi-detector CT images," *Medical Image Analysis*, vol. 73, p. 102166, 2021/10/01/ 2021, doi: <https://doi.org/10.1016/j.media.2021.102166>.
- [46] R. Tao, W. Liu, and G. Zheng, "Spine-transformers: Vertebra labeling and segmentation in arbitrary field-of-view spine CTs via 3D transformers," *Medical Image Analysis*, vol. 75, p. 102258, 2022.
- [47] Y. Deng *et al.*, "Ctspine1k: A large-scale dataset for spinal vertebrae segmentation in computed tomography," *arXiv preprint arXiv:2105.14711*, 2021.
- [48] Y. Mao, Q. Feng, Y. Zhang, and Z. Ning, "Semantics and instance interactive learning for labeling and segmentation of vertebrae in CT images," *Medical Image Analysis*, vol. 99, p. 103380, 2025.
- [49] I. D. Kawathekar, A. S. Areeckal, and V. Aparna, "A Novel Deep Learning Pipeline for Vertebra Labelling and Segmentation of Spinal Computed Tomography Images," *IEEE Access*, 2024.
- [50] J. L. Ba, J. R. Kiros, and G. E. Hinton, "Layer normalization," *arXiv preprint arXiv:1607.06450*, 2016.
- [51] N. Lessmann. *Normalized CT images and reference segmentations of thoracic and lumbar vertebrae from the CSI 2014 workshop*, doi: 10.5281/zenodo.7049844.
- [52] W. Li, Y. M. Tang, Z. Wang, K. M. Yu, and S. To, "Atrous residual interconnected encoder to attention decoder framework for vertebrae segmentation via 3D volumetric CT images," *Engineering Applications of Artificial Intelligence*, vol. 114, p. 105102, 2022.
- [53] S. F. Qadri, L. Shen, M. Ahmad, S. Qadri, S. S. Zareen, and M. A. Akbar, "SVseg: Stacked sparse autoencoder-based patch classification modeling for vertebrae segmentation," *Mathematics*, vol. 10, no. 5, p. 796, 2022.
- [54] P. Cheng, Y. Yang, H. Yu, and Y. He, "Automatic vertebrae localization and segmentation in CT with a two-stage Dense-U-Net," *Scientific Reports*, vol. 11, no. 1, p. 22156, 2021.
- [55] Z. Han, B. Wei, A. Mercado, S. Leung, and S. Li, "Spine-GAN: Semantic segmentation of multiple spinal structures," *Medical image analysis*, vol. 50, pp. 23-35, 2018.
- [56] Z. Wu *et al.*, "A novel 3D lumbar vertebrae location and segmentation method based on the fusion envelope of 2D hybrid visual projection images," *Computers in Biology and Medicine*, vol. 151, p. 106190, 2022.

[57] B. T. Di Muzio, Stefan; Mistry, Vikas; et al. "Maximum intensity projection." <https://radiopaedia.org/articles/14801> (accessed 2 March 2025).

[58] R. M. Haralick, K. Shanmugam, and I. H. Dinstein, "Textural features for image classification," *IEEE Transactions on systems, man, and cybernetics*, no. 6, pp. 610-621, 2007.

[59] S. Aja-Fernández, G. Ramos-Llordén, and P. A. Yushkevich, "Chapter 5 - Image representation and 2D signal processing," in *Medical Image Analysis*, A. F. Frangi, J. L. Prince, and M. Sonka Eds.: Academic Press, 2024, pp. 115-143.

[60] J. Redmon, "You only look once: Unified, real-time object detection," in *Proceedings of the IEEE conference on computer vision and pattern recognition*, 2016.

[61] Y. Zhao *et al.*, "Detrs beat yolos on real-time object detection," in *Proceedings of the IEEE/CVF Conference on Computer Vision and Pattern Recognition*, 2024, pp. 16965-16974.

[62] S. Zhang, C. Chi, Y. Yao, Z. Lei, and S. Z. Li, "Bridging the gap between anchor-based and anchor-free detection via adaptive training sample selection," in *Proceedings of the IEEE/CVF conference on computer vision and pattern recognition*, 2020, pp. 9759-9768.

[63] A. Wang *et al.*, "Yolov10: Real-time end-to-end object detection," *arXiv preprint arXiv:2405.14458*, 2024.

[64] N. Carion, F. Massa, G. Synnaeve, N. Usunier, A. Kirillov, and S. Zagoruyko, "End-to-end object detection with transformers," in *European conference on computer vision*, 2020: Springer, pp. 213-229.

[65] H. Rezatofighi, N. Tsoi, J. Gwak, A. Sadeghian, I. Reid, and S. Savarese, "Generalized intersection over union: A metric and a loss for bounding box regression," in *Proceedings of the IEEE/CVF conference on computer vision and pattern recognition*, 2019, pp. 658-666.

[66] P. Iakubovskii. "Segmentation Models Pytorch." GitHub. https://github.com/qubvel/segmentation_models.pytorch (accessed 26 January 2025).

[67] J. Deng, W. Dong, R. Socher, L.-J. Li, K. Li, and L. Fei-Fei, "Imagenet: A large-scale hierarchical image database," in *2009 IEEE conference on computer vision and pattern recognition*, 2009: Ieee, pp. 248-255.

[68] F. Milletari, N. Navab, and S.-A. Ahmadi, "V-net: Fully convolutional neural networks for volumetric medical image segmentation," in *2016 fourth international conference on 3D vision (3DV)*, 2016: Ieee, pp. 565-571.

[69] L. Fidon *et al.*, "Generalised wasserstein dice score for imbalanced multi-class segmentation using holistic convolutional networks," in *Brainlesion: Glioma, Multiple Sclerosis, Stroke and Traumatic Brain Injuries: Third International Workshop, BrainLes 2017, Held in Conjunction with MICCAI 2017, Quebec City, QC, Canada, September 14, 2017, Revised Selected Papers 3*, 2018: Springer, pp. 64-76.

[70] A. A. Taha and A. Hanbury, "Metrics for evaluating 3D medical image segmentation: analysis, selection, and tool," *BMC medical imaging*, vol. 15, no. 1, p. 29, 2015.

[71] Q. Ha. "RSNA 2022 Cervical Spine Fracture Detection 1st Place Solution." <https://www.kaggle.com/competitions/rsna-2022-cervical-spine-fracture-detection/writeups/qishen-ha-1st-place-solution> (accessed August 23, 2025).

[72] S. Hochreiter and J. Schmidhuber, "Long short-term memory," *Neural computation*, vol. 9, no. 8, pp. 1735-1780, 1997.

[73] A. Vaswani *et al.*, "Attention is all you need," *Advances in neural information processing systems*, vol. 30, 2017.

[74] M. Tan and Q. Le, "Efficientnetv2: Smaller models and faster training," in *International conference on machine learning*, 2021: PMLR, pp. 10096-10106.

[75] I. B. Goodfellow, Yoshua; Courville, Aaron, "Section 5.5: Estimators, Bias, and Variance," in *Deep Learning*: MIT Press, 2016, ch. 5.

[76] A. Holzinger, C. Biemann, C. S. Pattichis, and D. B. Kell, "What do we need to build explainable AI systems for the medical domain?," *arXiv preprint arXiv:1712.09923*, 2017.

[77] T. Miller, "Explanation in artificial intelligence: Insights from the social sciences," *Artificial intelligence*, vol. 267, pp. 1-38, 2019.

[78] K. Simonyan, A. Vedaldi, and A. Zisserman, "Deep inside convolutional networks: Visualising image classification models and saliency maps," *arXiv preprint arXiv:1312.6034*, 2013.

- [79] J. Vig, "A multiscale visualization of attention in the transformer model," *arXiv preprint arXiv:1906.05714*, 2019.
- [80] S. Wiegreffe and Y. Pinter, "Attention is not not explanation," *arXiv preprint arXiv:1908.04626*, 2019.
- [81] J. Cohen, "A coefficient of agreement for nominal scales," *Educational and psychological measurement*, vol. 20, no. 1, pp. 37-46, 1960.
- [82] J. L. Fleiss, "Measuring nominal scale agreement among many raters," *Psychological bulletin*, vol. 76, no. 5, p. 378, 1971.
- [83] R. Tian, G. Sun, X. Liu, and B. Zheng, "Sobel Edge Detection Based on Weighted Nuclear Norm Minimization Image Denoising," *Electronics*, vol. 10, no. 6, p. 655, 2021. [Online]. Available: <https://www.mdpi.com/2079-9292/10/6/655>.
- [84] J. Canny, "A computational approach to edge detection," *IEEE Transactions on pattern analysis and machine intelligence*, no. 6, pp. 679-698, 2009.
- [85] A. K. Jain and F. Farrokhnia, "Unsupervised texture segmentation using Gabor filters," *Pattern recognition*, vol. 24, no. 12, pp. 1167-1186, 1991.
- [86] A. F. Frangi, W. J. Niessen, K. L. Vincken, and M. A. Viergever, "Multiscale vessel enhancement filtering," in *International conference on medical image computing and computer-assisted intervention*, 1998: Springer, pp. 130-137.
- [87] S. G. Mallat, "A theory for multiresolution signal decomposition: the wavelet representation," *IEEE transactions on pattern analysis and machine intelligence*, vol. 11, no. 7, pp. 674-693, 2002.
- [88] P. Perona and J. Malik, "Scale-space and edge detection using anisotropic diffusion," *IEEE Transactions on pattern analysis and machine intelligence*, vol. 12, no. 7, pp. 629-639, 2002.
- [89] I. Sobel, "An isotropic 3×3 image gradient operator," *Machine vision for three-dimensional scenes*, pp. 376-379, 1990.
- [90] L. I. Rudin, S. Osher, and E. Fatemi, "Nonlinear total variation based noise removal algorithms," *Physica D: nonlinear phenomena*, vol. 60, no. 1-4, pp. 259-268, 1992.

Supplementary Materials

S1. Literature Review Summary

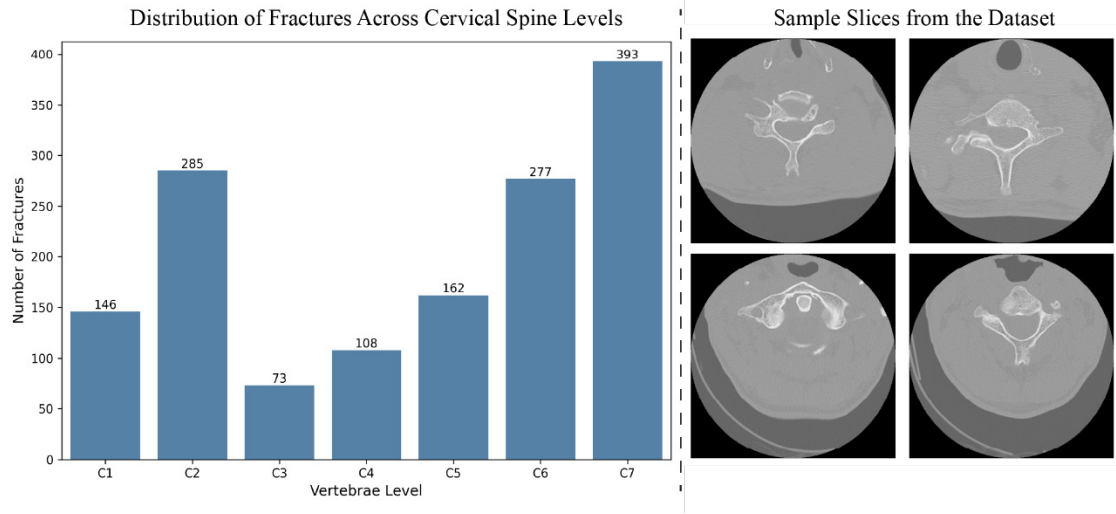
This section provides a detailed comparison of existing methodologies for cervical spine fracture detection. **Supplementary Table S1** summarizes key attributes of related studies, including dataset characteristics, validation strategies, and the specific level of detection (slice, vertebra, or patient). This comparison highlights critical gaps in the literature, particularly the prevalence of small, private datasets and balanced testing protocols that fail to reflect clinical reality.

Supplementary Table S1 Summary of cervical fracture detection studies

Study	Vertebra Identification	Fracture Localization	View	Level of detection	Explainability	Interobserver Variability	Cross Validation
Small et al. [24]	X	X	Axial	Slice	X	X	X
Esfahani et al. [25]	X	X	Axial	Slice	X	X	X
Bhavya et al. [3]	✓	X	3D	Vertebra & Patient	X	X	X
Nicolaes et al. [26]	✓	X	3D	Vertebra & Patient	X	X	✓
Rasul et al. [29]	X	X	Axial	Slice	X	X	X
Mahajan et al. [30]	X	X	Axial, Sagittal, Coronal	Patient	X	X	X
Chen et al. [31]	✓	X	3D	Vertebra	X	✓	X
Gaikwad et al. [4]	X	X	Axial	Slice	✓	X	X
Chlad et al. [35]	X	X	Axial	Slice	✓	X	X
Nejad et al. [36]	✓	✓	Axial	Slice	X	X	X
Boonrod et al. [37]	X	✓	Axial	Slice	X	✓	X
Yaseen et al. [39]	✓	X	Axial	Slice	✓	X	X
Golla et al. [20]	✓	✓	3D	Vertebra	✓	X	✓
Sutradhar et al. [18]	✓	✓	Axial, Sagittal, Coronal	Slice	✓	X	X
Tomita et al. [41]	X	X	Sagittal	Patient	✓	X	X
Salehinejad et al. [42]	X	X	3D, Axial	Slice, Patient	✓	X	✓
Hung et al. [19]	✓	✓	Axial 2.5D	Vertebra, Patient	X	X	✓

S2. Dataset Characteristics

This section presents a visual overview of the RSNA 2022 Cervical Spine Fracture dataset distribution and image characteristics. **Supplementary Figure S1** illustrates the frequency of fractures across the cervical vertebrae (C1–C7). The data reveals a significant class imbalance, with fractures occurring most frequently in C7 and C2, while the mid-cervical vertebrae (C3–C5) exhibit a notably lower prevalence. Additionally, representative CT slices are included to demonstrate the scan quality encountered within the patient cohort.



Supplementary Figure S1 Distribution of fractures per vertebra and example CT data from the dataset

S3. Mathematical Formulations of 2D Projections

This section provides detailed mathematical formulations for the projection techniques utilized in the pipeline, categorized by their specific application in either ROI detection or Vertebra Segmentation. Additionally, it elaborates on the rationale for the multi-label mask generation strategy.

S3.1. ROI Detection Projections

For the initial cervical spine localization, we investigated five fundamental projections suitable for capturing global anatomical structure. These correspond to the visual comparisons in **Supplementary Figure S2**.

- **Average Intensity Projection (AIP):** This computes the mean intensity value along the viewing axis.

$$I_{AIP}(x, y) = \mu(x, y) = \frac{1}{N} \sum_{z=1}^N I(x, y, z) \quad (S1)$$

- **Sum Projection:** This computes the sum of the intensity value along the viewing axis.

$$I_{Sum}(x, y) = \sum_{z=1}^N I(x, y, z) \quad (S2)$$

- **Gradient Projection:** This identifies edges using the Sobel filter and takes the maximum gradient value along the viewing axis. $G(I(x, y, z))$ is the gradient magnitude computed using the sobel operator. It computes the gradient in the x and y directions and combines them to determine the overall gradient magnitude [83].

$$I_{Gradient}(x, y) = \max_z G(I(x, y, z)) \quad (S3)$$

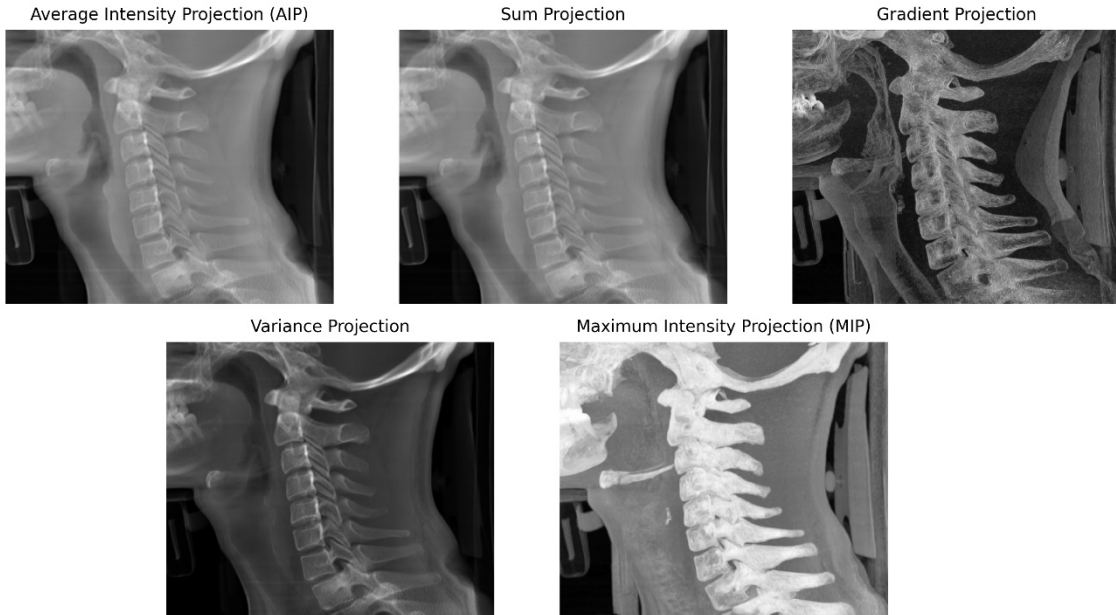
$$G(I(x, y, z)) = \sqrt{\left(\frac{\partial I(x, y, z)}{\partial x}\right)^2 + \left(\frac{\partial I(x, y, z)}{\partial y}\right)^2} \quad (S4)$$

- **Variance Projection:** This computes the variance of intensity along the viewing axis.

$$I_{\text{Variance}}(x, y) = \frac{1}{N} \sum_{z=1}^N (I(x, y, z) - \mu(x, y))^2 \quad (S5)$$

- **Maximum Intensity Projection (MIP):** This computes the maximum of the intensity value along the viewing axis.

$$I_{\text{MIP}}(x, y) = \max_z I(x, y, z) \quad (S6)$$



Supplementary Figure S2 Projections analyzed for cervical spine ROI detection

S3.1. Segmentation Projections

For the vertebra segmentation phase, which requires precise boundary delineation, we expanded the investigation to include texture, statistical, and filter-based projections. These definitions correspond to the visual comparisons in **Supplementary Figure S3** (Sagittal) and **Supplementary Figure S4** (Coronal).

- **Difference Projection:** Highlights sudden changes in intensity between adjacent slices, useful for identifying discontinuities.

$$I_{\text{Difference}}(x, y) = \sum_{z=1}^{N-1} |I(x, y, z + 1) - I(x, y, z)| \quad (S7)$$

- **Energy Projection:** Computes the sum of squared intensities across slices, highlighting high-intensity regions [58].

$$I_{\text{Energy}}(x, y) = \sum_{z=1}^N I(x, y, z)^2 \quad (\text{S8})$$

- **Gradient Magnitude Projection:** Calculates the gradient magnitude for each slice and sums it across slices, emphasizing edges and boundaries.

$$I_{\text{Grad_mag}}(x, y) = \sum_{z=1}^N \sqrt{\left(\frac{\partial I(x, y, z)}{\partial x}\right)^2 + \left(\frac{\partial I(x, y, z)}{\partial y}\right)^2} \quad (\text{S9})$$

- **Kurtosis Projection:** Measures the "tailedness" of the intensity distribution across slices, useful for capturing extreme intensity variations.

$$I_{\text{Kurtosis}}(x, y) = \frac{\frac{1}{N} \sum_{z=1}^N (I(x, y, z) - \mu(x, y))^4}{\left(\frac{1}{N} \sum_{z=1}^N (I(x, y, z) - \mu(x, y))^2\right)^2} \quad (\text{S10})$$

- **Median Projection:** Computes the median intensity across slices.

$$I_{\text{Median}}(x, y) = \text{median}_z I(x, y, z) \quad (\text{S11})$$

- **Percentile Range Projection:** Measures the difference between two percentiles, highlighting intensity variation within a specific range. We have used the 95th and the 5th percentiles. Here P_x is xth percentile function.

$$I_{\text{PercentileRange}}(x, y) = P_{95}(x, y) - P_5(x, y) \quad (\text{S12})$$

- **Skewness Projection:** Captures the asymmetry of intensity distribution across slices, useful for identifying biased intensity patterns.

$$I_{\text{Skewness}}(x, y) = \frac{\mu_3}{\sigma^3}, \quad \mu_3 = \frac{1}{N} \sum_{z=1}^N (I(x, y, z) - \mu)^3 \quad (\text{S13})$$

- **Standard Deviation Projection:** Measures the spread of intensity values across slices.

$$I_{\text{StdDev}}(x, y) = \sqrt{\frac{1}{N} \sum_{z=1}^N (I(x, y, z) - \mu(x, y))^2} \quad (\text{S14})$$

- **Edge Detection Projection:** Highlights edges by summing edge-detected slices. Where $C(I)$ is the Canny edge detection function [84].

$$I_{\text{Edge}}(x, y) = C(I(x, y, z)) \quad (\text{S15})$$

- **Gabor Projection:** Enhances texture patterns by applying Gabor filters to each slice. Here $g(x, y)$ is a 2D Gabor filter kernel [85].

$$I_{\text{Gabor}}(x, y) = \sum_{z=1}^N \int \int I(x, y, z) g(x, y) dx dy \quad (\text{S16})$$

- **Frangi Projection:** Enhances tubular structures, useful for visualizing elongated features. Here, λ_1 and λ_2 are the eigenvalues of the hessian matrix at a pixel. β and γ are tuning parameters [86].

$$I_{\text{Frangi}}(x, y) = \sum_{z=1}^N \exp \left(-\frac{\lambda_1^2}{2\beta^2} - \frac{\lambda_2^2}{2\gamma^2} \right) \quad (\text{S17})$$

- **Hessian Projection:** Highlights curvilinear structures by computing the determinant of the Hessian matrix. Where H is the Hessian determinant [86].

$$I_{\text{Hessian}}(x, y) = \sum_{z=1}^N H(I(x, y, z)) \quad (\text{S18})$$

- **Wavelet Projection:** Applies wavelet transformation to capture multi-resolution features. $\psi_{m,n}$ is the wavelet function [87].

$$I_{\text{Wavelet}}(x, y) = \sum_{z=1}^N \sum_{m,n} \psi_{m,n} I(x, y, z) \quad (\text{S19})$$

- **Anisotropic Diffusion Projection:** Smooths slices while preserving edges, emphasizing large-scale features [88].

$$I_{\text{Diffusion}}(x, y) = \sum_{z=1}^N \nabla \cdot (D \nabla I(x, y, z)) \quad (\text{S20})$$

- **Nonlinear Enhancement Projection:** Enhances high-intensity areas using a nonlinear power function.

$$I_{\text{Nonlinear}}(x, y) = \frac{1}{N} \sum_{z=1}^N I(x, y, z)^p \quad (\text{S21})$$

- **Texture Energy Projection:** Captures texture patterns using energy from specific filters .

$$I_{\text{Texture}}(x, y) = \sum_{z=1}^N \sqrt{\left(\frac{\partial^2 I}{\partial x^2} \right)^2 + \left(\frac{\partial^2 I}{\partial y^2} \right)^2} \quad (\text{S22})$$

- **Standardized Projection:** Standardizes intensity values across slices to emphasize relative differences.

$$I_{\text{Standardized}}(x, y) = \frac{I(x, y, z) - \mu(x, y)}{\sigma(x, y)} \quad (\text{S23})$$

- **Intensity Inversion Projection:** Inverts intensity values to highlight low-intensity regions.

$$I_{\text{Inverted}}(x, y) = \max_z I(x, y, z) - I(x, y, z) \quad (\text{S24})$$

- **Sobel Edge Projection:** Highlights edges using the Sobel operator [89].

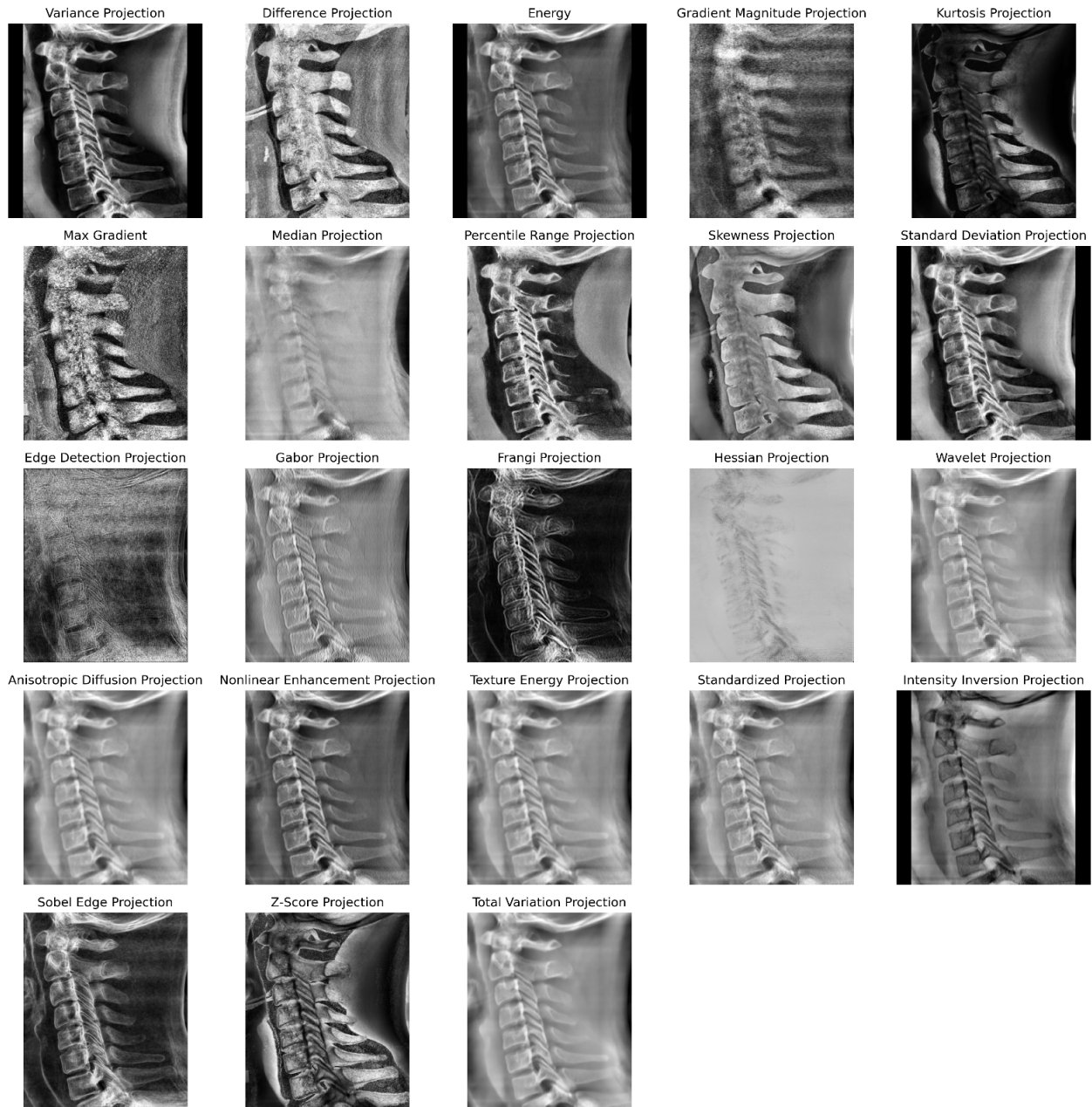
$$I_{\text{Sobel}}(x, y) = \sum_{z=1}^N \sqrt{\left(\frac{\partial I(x, y, z)}{\partial x} \right)^2 + \left(\frac{\partial I(x, y, z)}{\partial y} \right)^2} \quad (\text{S25})$$

- **Z-Score Projection:** Emphasizes areas with extreme intensity deviations using z-scores.

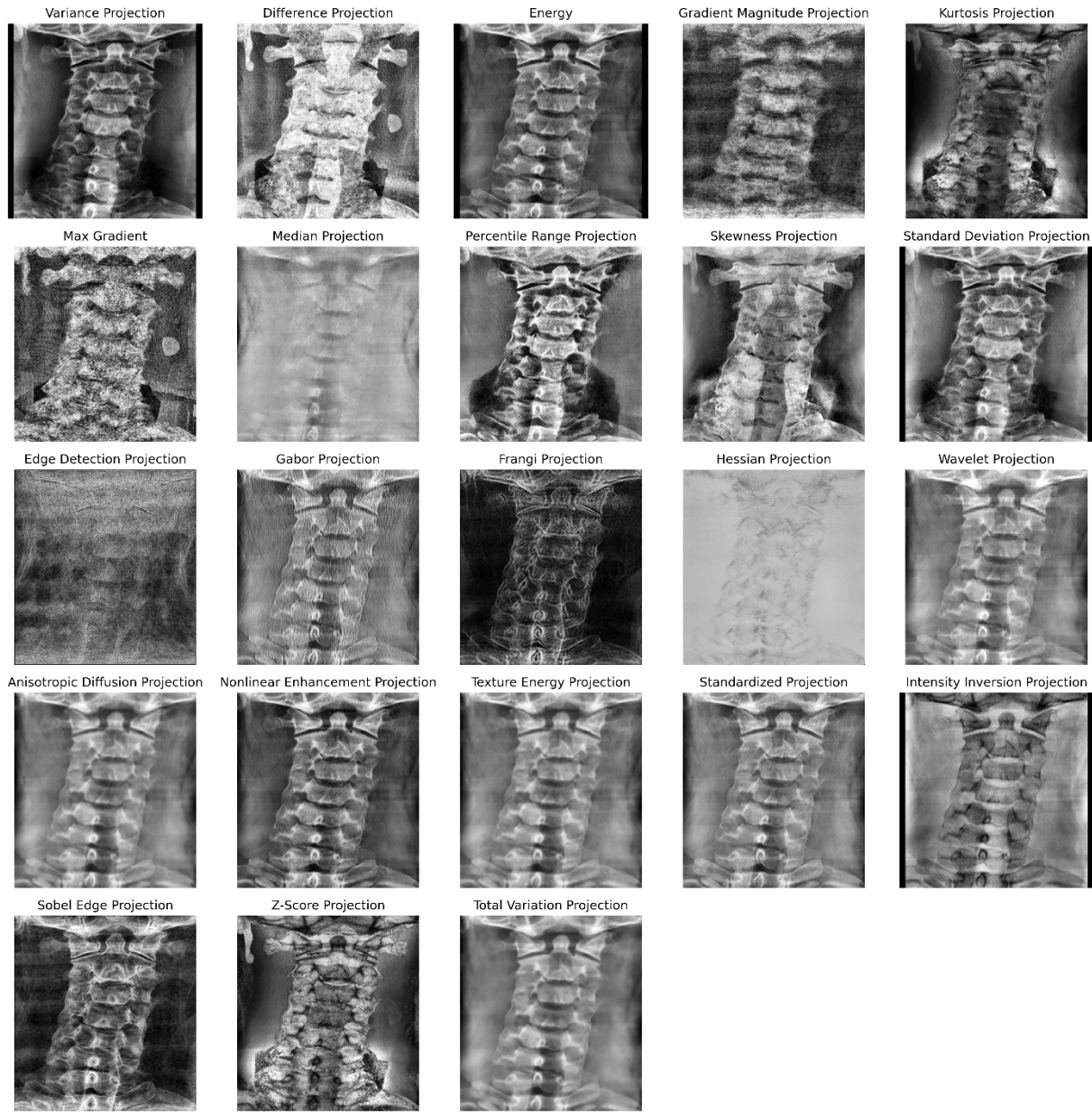
$$I_{\text{ZScore}}(x, y) = \frac{I(x, y, z) - \mu(x, y)}{\sigma(x, y)} \quad (\text{S26})$$

- **Total Variation Projection:** Minimizes noise while preserving structural details [90].

$$I_{\text{TotalVariation}}(x, y) = \sum_{z=1}^N |\nabla I(x, y, z)| \quad (\text{S27})$$



Supplementary Figure S3 Sagittal projections analyzed for vertebra segmentation



Supplementary Figure S4 Coronal projections analyzed for vertebra segmentation

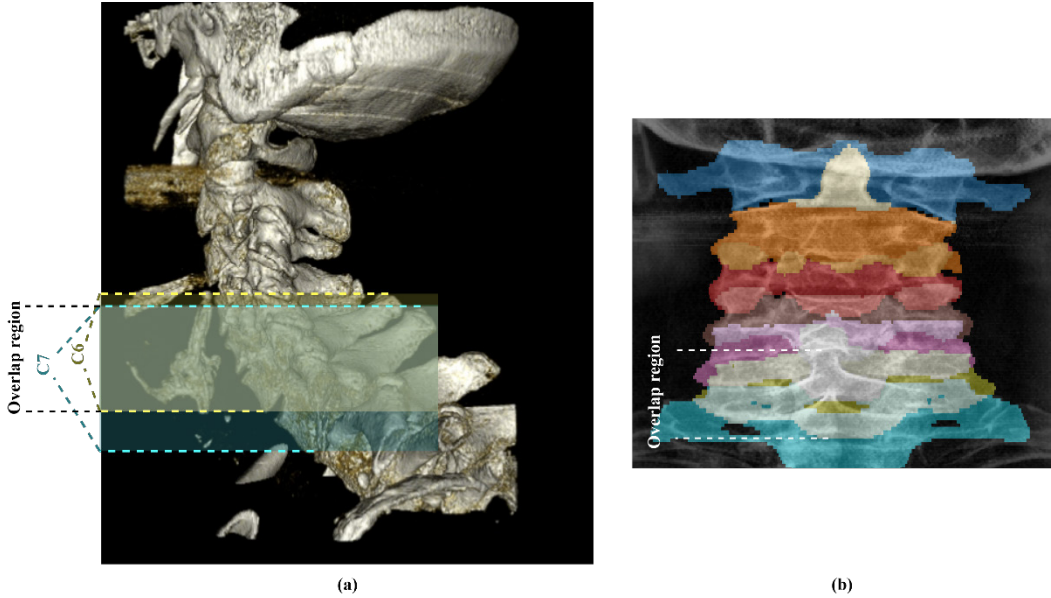
S4. Methodological Elaborations

This section provides supplementary details regarding the rationale behind the segmentation strategy, the mathematical definitions of the loss functions and metrics used for evaluation, and the specific architectures of the baseline models (2D and 3D) used for performance comparison.

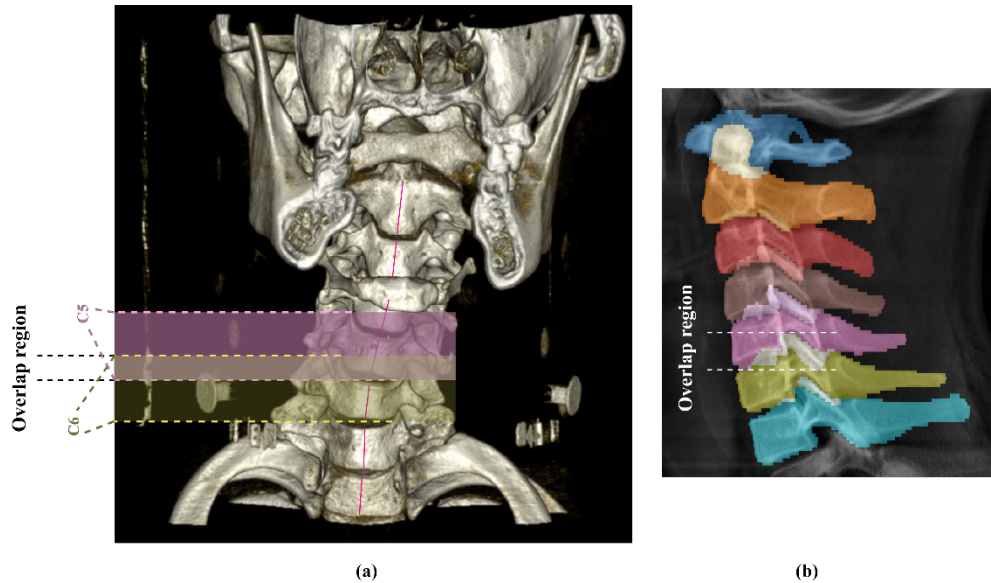
S4.1. Justification for Multi-label Mask Generation

Since we are attempting to perform segmentation from the coronal and sagittal projections of the cervical spine VOI, some of the anatomical features of the spine overlap when viewing from such orthogonal views. Due to this overlap, a single pixel in the projection image can belong to two vertebrae that are overlapping from the orthogonal perspective. Most patients in the RSNA dataset do not have straight necks. So the spinous process of a vertebra can overlap the vertebral body of neighboring vertebra. **Supplementary Figure S5** demonstrates the overlap between

C6 and C7 vertebrae. As the spinous process of C7 is directly behind the vertebral body of C6 due to the curvature of the neck, when viewed from the coronal perspective the vertebra masks will overlap. We can see the overlap in the coronal projection in **Supplementary Figure S5 (b)**. **Supplementary Figure S6** demonstrates a patient with bent neck visible from the coronal perspective. The centerline of the neck is roughly shown with red lines. The transverse process and vertebral bodies of neighboring C5 and C6 vertebra show overlap when viewed from the sagittal perspective which is visible in sagittal projection shown in **Supplementary Figure S6 (b)**.



Supplementary Figure S5 Overlap in the coronal projection (a) CT Volume (b) Multilabel Mask



Supplementary Figure S6 Overlap in the sagittal projection (a) CT Volume (b) Multilabel Mask

Due to these overlaps a normal multi-class segmentation was not suitable for this study. Hence, we proposed a multi-label segmentation approach where the same pixel in the projection can belong to multiple classes. This multi-label mask has been constructed by filtering only cervical vertebrae (C1-C7) from the provided 3D multi-class mask of the cervical spine. Then the max projection of each vertebra was taken in the direction of the projection and the binary masks of each vertebra were stacked in separate layers.

S4.2. Loss Function and Evaluation metrics

ROI Detection:

Here are formulation of evaluation metrics for ROI detection:

$$IoU_i = \frac{\text{Area of } (P_i \cap G_i)}{\text{Area of } (P_i \cup G_i)} \quad (\text{S28})$$

$$mIoU = \frac{1}{N} \sum_{i=1}^N IoU_i \quad (\text{S29})$$

Vertebra Segmentation:

We utilized a combined loss function leveraging both Dice and Jaccard losses to balance overlap optimization and false positive penalization. Here are the loss function and evaluation metric formulation for segmentation.

$$L_{\text{Dice}} = 1 - \frac{2 \sum_{i=1}^N \sum_{j=1}^C y_{i,j} p_{i,j} + \epsilon}{\sum_{i=1}^N \sum_{j=1}^C (y_{i,j} + p_{i,j}) + \epsilon} \quad (\text{S30})$$

$$L_{\text{Jaccard}} = 1 - \frac{\sum_{i=1}^N \sum_{j=1}^C y_{i,j} p_{i,j} + \epsilon}{\sum_{i=1}^N \sum_{j=1}^C (y_{i,j} + p_{i,j} - y_{i,j} p_{i,j}) + \epsilon} \quad (\text{S31})$$

$$L_{\text{Combined}} = \frac{L_{\text{Dice}} + L_{\text{Jaccard}}}{2} \quad (\text{S32})$$

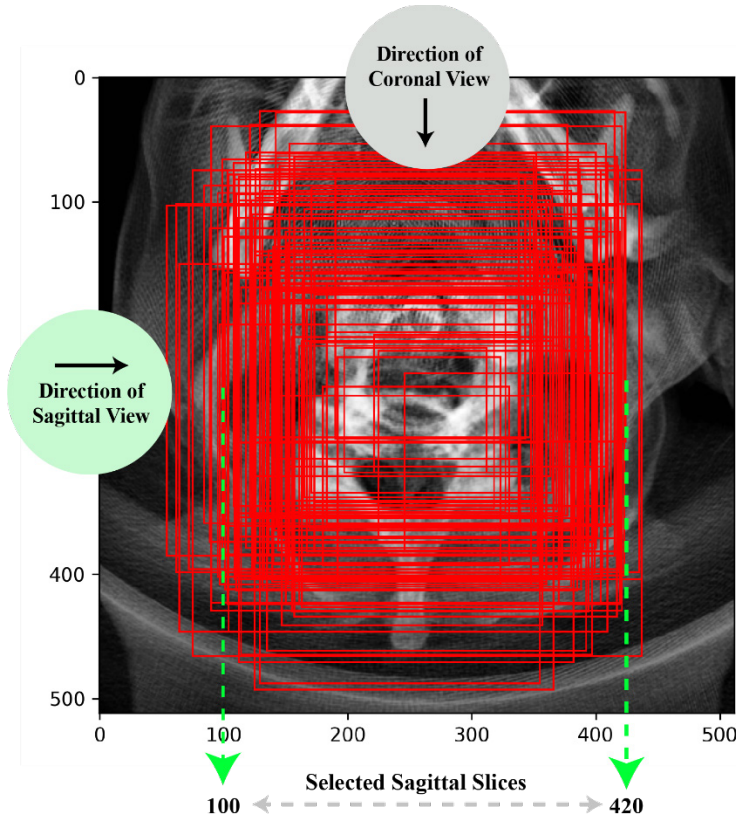
$$IoU = \frac{TP}{TP + FP + FN} \quad (\text{S33})$$

$$DSC = \frac{2TP}{2TP + FP + FN} \quad (\text{S34})$$

$$\begin{aligned} & \text{HausdorffDistance, } H(A, B) \\ &= \max \left(\max_{a \in A} \left\{ \min_{b \in B} |a - b| \right\}, \max_{b \in B} \left\{ \min_{a \in A} |b - a| \right\} \right) \end{aligned} \quad (\text{S35})$$

S4.3. Heuristic Slice Selection Strategy

To optimize computational efficiency, we employed a heuristic slice selection strategy to prune the input volumes. By plotting the bounding boxes of the cervical spine across the dataset, we visually determined that the relevant anatomy is consistently contained within the central sagittal slices. Based on this observation, we cropped the volume to include only slice indices 100 to 420 (as shown in the top of **Supplementary Figure S7**). This was identified as a safe choice to exclude irrelevant peripheral anatomy (such as shoulders) without risking the loss of vertebral data.



Supplementary Figure S7 Heuristic selection of Sagittal Slices

S4.4. Baseline Fracture Identification Architectures

To validate the efficacy of our proposed 2.5D Spatio-Sequential model, we implemented and evaluated two alternative architectural paradigms: a direct 2D projection approach and a full 3D volumetric approach.

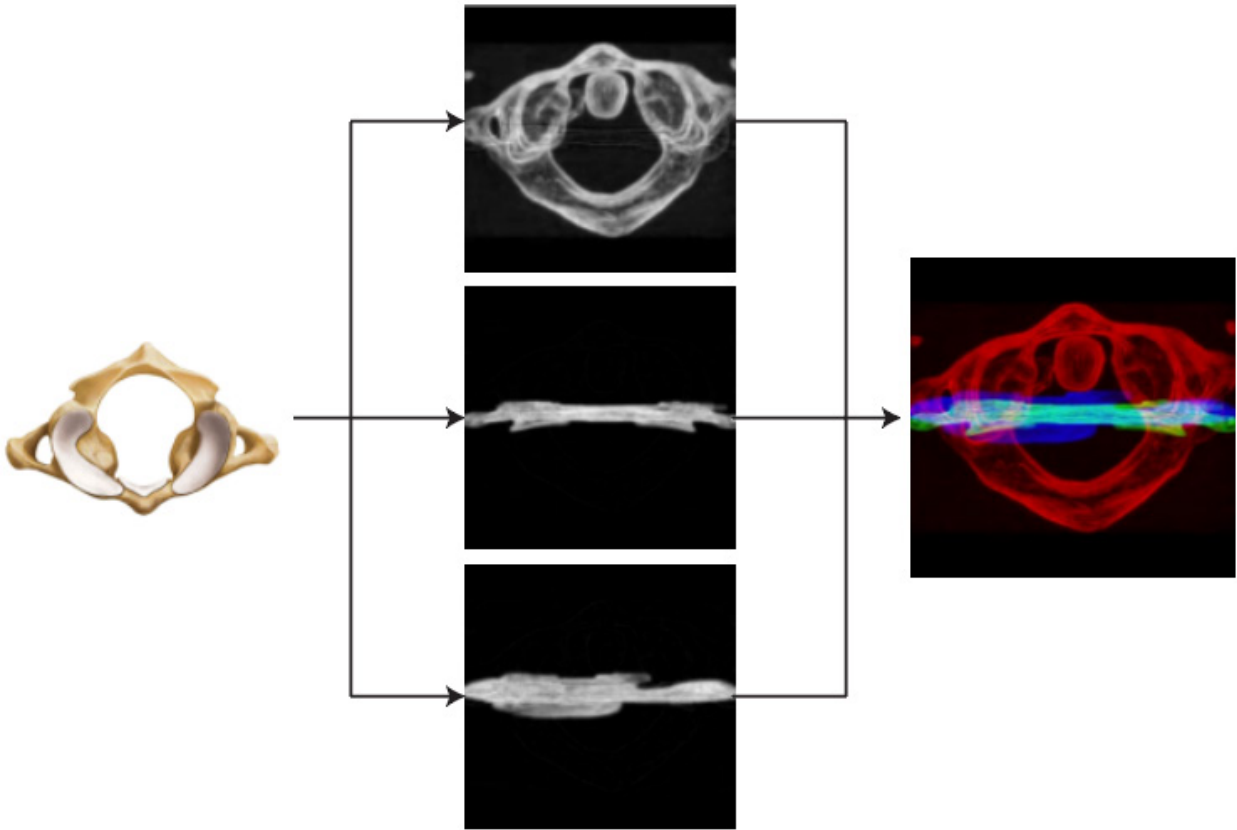
S4.4.1 Directly Projection-Based 2D Networks

This approach simulates a radiologist's workflow of assessing fractures from multiple 2D views.

- **Input & Preprocessing:** We utilized variance projections of the vertebrae from axial, sagittal, and coronal perspectives. A bone window (400 HU width, 1400 HU level) was applied prior to projection to enhance visibility.
- **Fusion Strategy:** For vertebra-level classification, the three orthogonal projections were resized and stacked along the channel axis to form a composite RGB input, providing the model with simultaneous

multi-view context (see **Supplementary Figure S9**). For patient-level classification, we employed score-level fusion, combining predictions from sagittal and coronal views via weighted averaging.

- **Architectures:** We evaluated standard CNN backbones including ResNet50, DenseNet121, and MobileNetV2, alongside a custom 3-layer CNN.



Supplementary Figure S8 Multi-channel projection strategy stacking axial, sagittal, and coronal views for vertebra-level classification

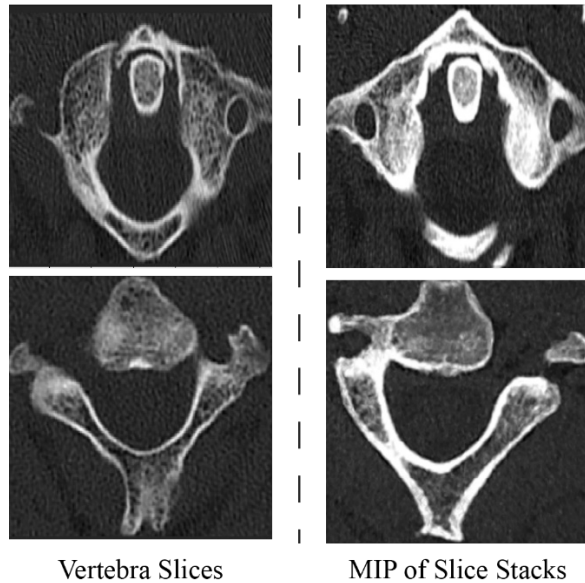
S4.4.2 Full-Volume 3D CNN Networks

This approach utilizes the entire 3D volume of the segmented vertebra, preserving full spatial context at the cost of computational intensity.

- **Preprocessing:** Vertebrae volumes were extracted and preprocessed with a bone window. Unlike the projection methods, we preserved the full volumetric depth (slice count) and applied 3D-specific augmentations such as random rotation and elastic deformation to improve generalization.
- **Architecture:** We employed an EfficientNet-B0 backbone adapted for 3D inputs using 3D convolutional kernels. The model processes the full voxel grid in a channel-first format to extract hierarchical spatial features across all dimensions.
- **Limitation:** While theoretically providing the richest context, this method proved prone to overfitting due to the high dimensionality of the input space relative to the available training data.

S4.5 Input Preprocessing for 2.5D Networks

To generate the inputs for the 2.5D Spatio-Sequential networks, we processed the raw CT volumes into 2D projections. **Supplementary Figure S9** compares the raw vertebral slices against the Maximum Intensity Projections (MIP) of the slice stacks. This preprocessing step effectively condenses volumetric information, enhancing the visibility of dense bone structures while suppressing soft tissue variation. This creates a high-contrast representation optimized for the classification model.



Supplementary Figure S9 Example of 2.5D Network Input Data (single slices are shown instead of stacks)

S5. Extended Results: Cervical Spine VOI Detection

This section presents the complete quantitative results for the cervical spine Region of Interest (ROI) detection experiments. All models were evaluated using 5-fold cross-validation on the subset of 87 patients with ground truth segmentation masks.

S5.1. Quantitative Comparison of Detection Models

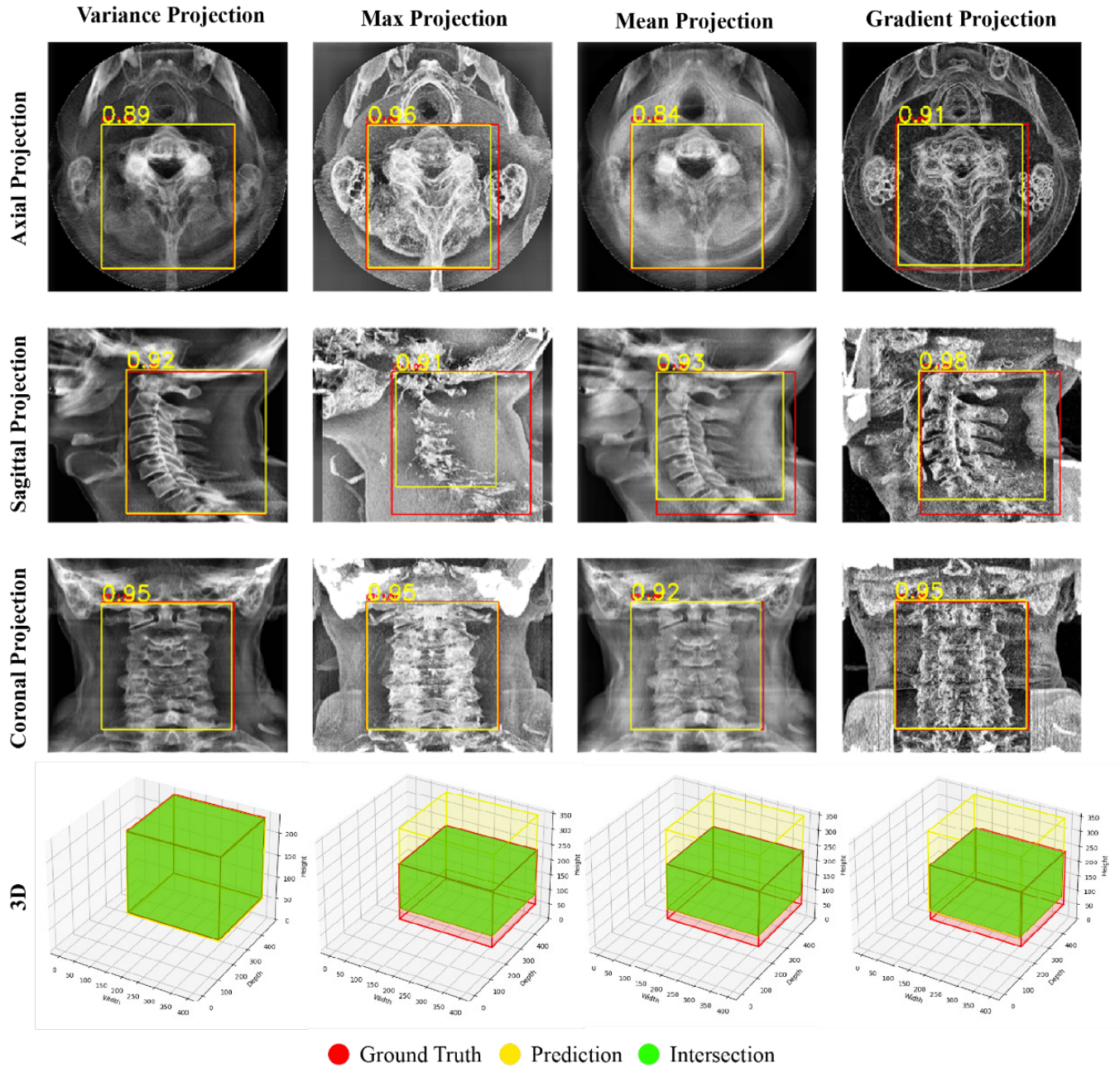
Supplementary Table S2 provides the detailed performance metrics (Sagittal, Coronal, Axial, and 3D Mean IoU) for all evaluated object detection architectures (YOLOv5, YOLOv8, YOLOv9, YOLOv10, and RT-DETR) across four different projection techniques.

Supplementary Table S2 Model Performance Comparison for Cervical Spine Detection across different projection types

Projection	Model	Sagittal mIOU	Coronal mIOU	Axial mIOU	3D mIOU
Max	YOLOv8m	87.01	96.33	92.53	88.67
	YOLOv8l	87.33	96.47	89.31	87.10
	YOLOv8x	85.09	94.94	92.58	87.50
	YOLOv5m	86.57	96.11	93.76	89.57
	YOLOv5l	90.30	96.15	90.48	90.04
	YOLOv5x	89.22	96.14	92.13	90.16
	RTDETR-1	89.83	92.29	89.55	87.59

	RTDETR-x	88.70	90.94	90.04	86.93
	YOLOv9c	86.88	95.18	89.50	87.45
	YOLOv10m	86.34	94.07	88.94	86.81
	YOLOv10x	85.55	93.88	92.45	87.69
Mean	YOLOv8m	90.56	94.90	92.34	90.46
	YOLOv8l	88.69	95.17	90.94	88.85
	YOLOv8x	92.15	95.37	91.80	91.40
	YOLOv5m	89.39	94.88	91.66	89.73
	YOLOv5l	90.48	95.36	93.03	91.31
	YOLOv5x	90.09	96.17	92.61	90.78
	RTDETR-1	90.70	91.35	87.44	87.36
	RTDETR-x	90.85	88.68	88.64	86.72
	YOLOv9c	90.64	93.55	90.37	89.22
	YOLOv10m	88.22	94.02	90.50	89.05
	YOLOv10x	89.31	95.03	90.47	89.07
Variance	YOLOv8m	95.50	95.96	92.88	93.33
	YOLOv8l	95.99	96.41	93.17	93.84
	YOLOv8x	95.64	96.35	94.79	94.45
	YOLOv5m	95.64	96.11	93.66	93.97
	YOLOv5l	94.89	96.09	94.40	93.89
	YOLOv5x	95.30	96.79	93.05	93.75
	RTDETR-1	92.29	92.76	89.91	89.95
	RTDETR-x	91.53	91.74	89.81	89.21
	YOLOv9c	93.45	95.10	93.04	92.25
	YOLOv10m	94.61	95.09	92.21	92.45
	YOLOv10x	93.17	95.06	92.77	92.06
Grad	YOLOv8m	88.92	96.06	91.93	89.94
	YOLOv8l	86.93	95.83	92.97	88.58
	YOLOv8x	88.94	95.66	89.66	89.22
	YOLOv5m	87.34	95.77	89.72	88.15
	YOLOv5l	87.93	95.55	91.92	89.39
	YOLOv5x	88.06	95.93	93.01	89.84
	RTDETR-1	89.08	92.88	88.62	87.23
	RTDETR-x	89.50	92.69	87.40	87.72
	YOLOv9c	85.48	94.18	90.97	87.29
	YOLOv10m	89.32	92.91	91.99	89.53
	YOLOv10x	81.86	95.26	89.41	84.37

Supplementary Figure S10 illustrates the qualitative impact of the projection method on localization accuracy. The variance projection consistently produced the most robust features, enabling the model to ignore soft tissue noise that often confounds the Max (MIP) and Mean projections



Supplementary Figure S10 Cervical Spine Location Predictions of YOLOv8x across all projections

S5.2. Ablation Study: Effect of Interpolation

We investigated the impact of slice interpolation on detection performance. **Supplementary Table S3** summarizes the results, demonstrating that interpolation consistently improved the 3D mIOU across almost all model architectures, with the best-performing model (YOLOv8x) improving from 93.46% to 94.45%.

Supplementary Table S3 Effect of Interpolation on Performance

Interpolation	Model	Sagittal		Coronal		Axial		3D
		mAP	mIOU	mAP	mIOU	mAP	mIOU	mIOU
No	YOLOv8m	95.56	95.06	96.79	95.99	55.65	93.01	93.47
	YOLOv8l	94.65	94.51	96.44	95.97	53.64	92.58	93.01
	YOLOv8x	95.73	95.06	96.61	95.96	56.08	93.20	93.46
	YOLOv5m	95.74	94.93	96.25	95.75	55.25	94.32	93.81
	YOLOv5l	96.00	95.27	94.41	95.04	58.81	93.53	93.21
	YOLOv5x	95.00	94.61	97.17	95.76	58.73	93.86	93.35
	RTDETR-l	87.94	92.43	89.90	93.63	44.88	86.92	88.64
	RTDETR-x	86.34	91.44	86.73	92.11	48.44	85.19	87.30
	YOLOv9c	94.65	94.62	93.60	94.75	52.48	91.82	92.30
	YOLOv10m	93.01	94.32	93.93	94.99	54.58	93.08	92.89
Yes	YOLOv10x	88.51	93.11	94.85	95.53	52.15	91.21	91.38
	YOLOv8m	96.78	95.50	96.51	95.96	61.26	92.88	93.33
	YOLOv8l	97.19	95.99	96.98	96.41	59.53	93.17	93.84
	YOLOv8x	95.83	95.64	97.38	96.35	60.26	94.79	94.45
	YOLOv5m	97.34	95.64	96.78	96.11	59.07	93.66	93.97
	YOLOv5l	95.50	94.89	96.68	96.09	59.30	94.40	93.89
	YOLOv5x	95.97	95.30	98.50	96.79	60.95	93.05	93.75
	RTDETR-l	87.95	92.29	88.93	92.76	53.68	89.91	89.95
	RTDETR-x	86.98	91.53	84.29	91.74	55.32	89.81	89.21
	YOLOv9c	92.13	93.45	94.76	95.10	58.12	93.04	92.25
	YOLOv10m	93.24	94.61	93.71	95.09	54.17	92.21	92.45
	YOLOv10x	90.16	93.17	93.36	95.06	58.35	92.77	92.06

S6. Extended Results: Multi-label Segmentation

This section details the comprehensive performance evaluation of the multi-label vertebra segmentation stage. We report the comparative results for different deep learning architectures, the exhaustive benchmark of projection techniques, and the ablation studies justifying our preprocessing choices.

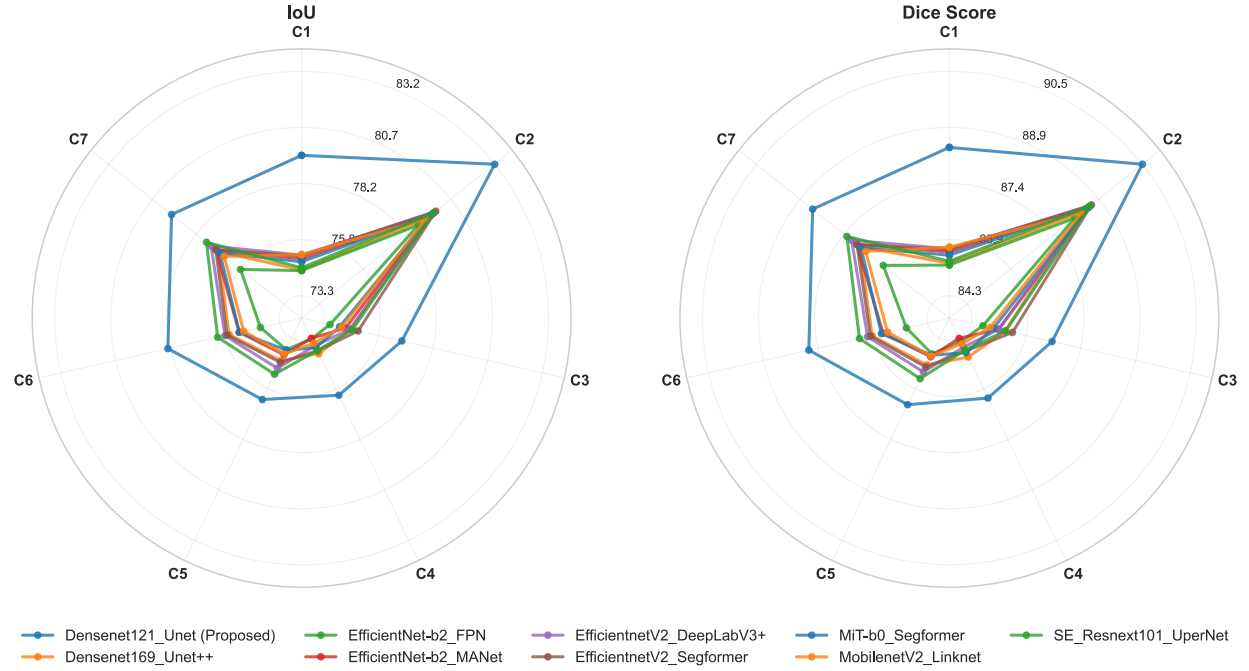
S6.1 Comparative Analysis of Segmentation Models

To assess model robustness across varying anatomical geometries, we analyzed the Intersection over Union (IoU) and Dice Score (DSC) for each individual vertebra (C1–C7). **Supplementary Figure S11** presents this comparison in a radar plot format.

The proposed DenseNet121-Unet (represented by the blue line) consistently traces the outermost perimeter of the plot, indicating superior performance across every cervical level compared to baseline models like SegFormer and DeepLabV3+. Notably, while several competing models exhibit a significant contraction (performance drop) at C1 (Atlas), the proposed model maintains high accuracy, suggesting it effectively captures the unique ring-like morphology of the atlas that others struggle to define.

A common trend observed across all architectures is a visible dip in performance for the mid-cervical vertebrae (C3–C5), represented by the inward retraction of the lines toward the center. This visualizes the inherent difficulty

in segmenting these anatomically compressed and structurally similar vertebrae. Despite this challenge, the DenseNet121-Unet maintains the largest coverage area even in these regions, confirming its stability relative to the state-of-the-art.



Supplementary Figure S11 Vertebra wise performance comparison radar plot

S6.2 Comprehensive Benchmark of Projection Techniques

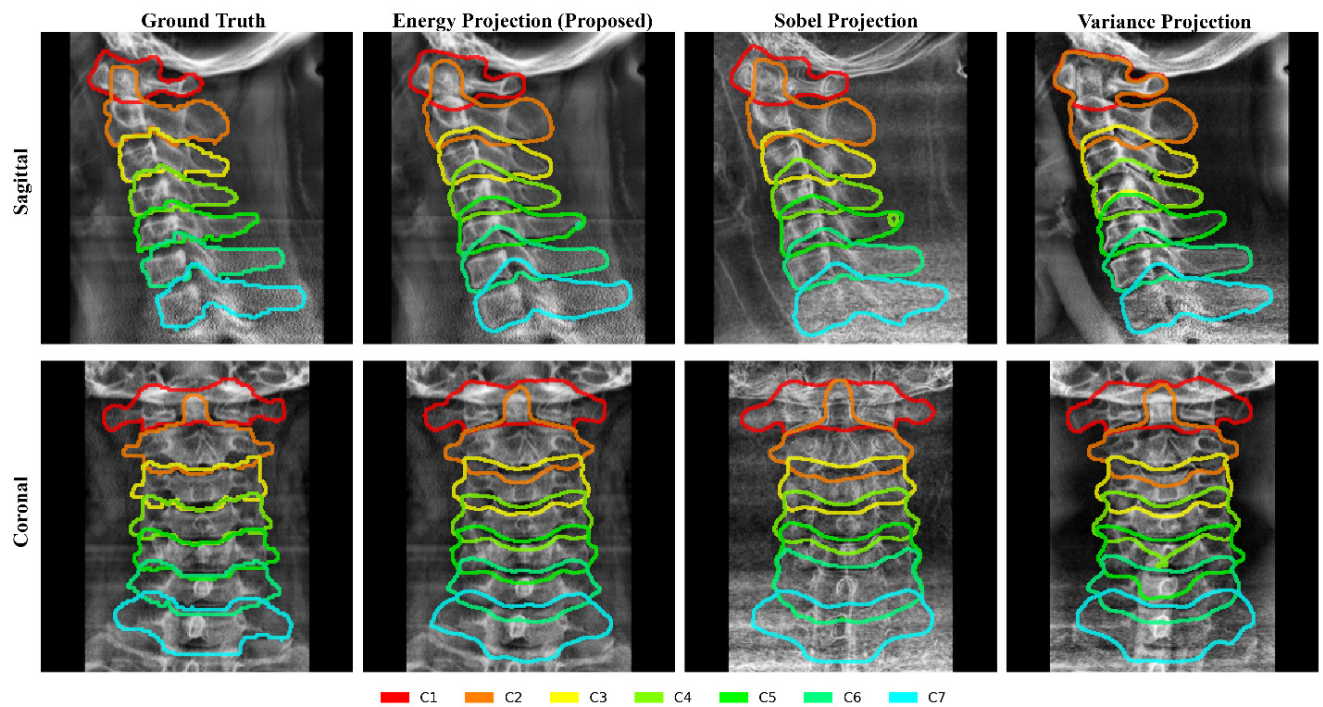
To determine the most effective 2D representation for segmentation, we conducted an exhaustive comparison of 23 different projection techniques. **Supplementary Table S4** summarizes the results. The Energy projection achieved the highest composite score (1.48) and the lowest Hausdorff Distance (4.50 mm), indicating it provides the best boundary definition.

Supplementary Table S4 Performance Comparison Among Different Projections

Projection	Sagittal			Coronal			Average			Score↑
	IoU↑	Dice↑	HD95↓	IoU↑	Dice↑	HD95↓	IoU↑	Dice↑	HD95↓	
Diffusion	73.27	84.36	6.50	76.84	86.77	5.15	75.06	85.57	5.82	1.21
Difference	71.74	83.07	8.82	75.28	85.70	6.65	73.51	84.38	7.74	0.91
Edge	64.39	77.93	10.14	69.03	81.49	9.73	66.71	79.71	9.94	0.44
Energy	78.53	87.93	4.17	78.36	87.79	4.83	78.45	87.86	4.50	1.48
Frangi	69.32	81.58	8.03	72.66	84.08	6.60	70.99	82.83	7.31	0.91
Gabor	71.08	82.76	7.94	74.25	84.97	6.59	72.67	83.86	7.26	0.96
Gradient	62.17	76.36	11.44	70.66	82.65	7.60	66.41	79.51	9.52	0.50
Hessian	60.94	75.39	11.70	68.24	80.91	9.40	64.59	78.15	10.55	0.31
Inversion	76.29	86.50	5.03	76.27	86.41	5.16	76.28	86.46	5.09	1.35
Kurt	69.85	81.88	9.85	75.35	85.89	5.98	72.60	83.89	7.92	0.86
Max Gradient	66.44	79.31	9.60	70.84	82.83	7.96	68.64	81.07	8.78	0.65
Median	67.13	80.04	8.27	72.23	83.76	6.74	69.68	81.90	7.50	0.86
Nonlinear	76.95	86.76	5.10	75.41	85.74	6.19	76.18	86.25	5.65	1.26

Percentile Range	70.91	82.45	8.75	76.17	86.34	5.46	73.54	84.40	7.11	1.00
Skew	73.82	84.60	7.17	74.39	85.14	7.47	74.11	84.87	7.32	0.98
Sobel	72.93	84.16	6.63	73.55	84.62	6.30	73.24	84.39	6.47	1.08
Standardized	71.58	83.17	7.94	76.08	86.25	5.47	73.83	84.71	6.71	1.06
Standard Deviation	76.51	86.48	5.70	77.40	87.10	5.23	76.95	86.79	5.47	1.31
Texture Energy	74.65	85.42	5.71	76.04	86.25	5.51	75.35	85.84	5.61	1.25
Total Variance	74.33	84.95	6.37	75.53	85.88	5.94	74.93	85.42	6.16	1.16
Variance	75.69	86.00	6.31	77.43	87.23	5.34	76.56	86.62	5.82	1.25
Wavelet	72.67	83.96	6.23	74.36	85.06	6.85	73.52	84.51	6.54	1.08
Z score	73.08	84.03	8.10	77.89	87.50	4.85	75.49	85.76	6.48	1.13

Supplementary Figure S12 provides a qualitative confirmation of these metrics. The Energy projection allows the model to generate smooth, accurate masks, whereas edge-based methods like Sobel result in fragmented and noisy segmentations.



Supplementary Figure S12 Side by Side Segmentation Performance Comparison for Different Projections

S6.3 Impact of Preprocessing on Segmentation

We investigated the impact of two critical preprocessing steps: bone windowing and volume interpolation.

Supplementary Table S5 demonstrates that applying a bone window (800–1400 HU) prior to projection increased the average Dice score by 1.82% and reduced the HD95 from 6.09 to 4.50, significantly improving boundary fidelity .

Supplementary Table S5 Impact of Windowing in Segmentation Performance

Windowing	Sagittal			Coronal			Average		
	IoU↑	Dice↑	HD95↓	IoU↑	Dice↑	HD95↓	IoU↑	Dice↑	HD95↓
N/A	76.04	86.20	5.46	75.67	85.88	6.72	75.85	86.04	6.09
Bone Window	78.53	87.93	4.17	78.36	87.79	4.83	78.45	87.86	4.50

Supplementary Table S6 confirms that volume interpolation is essential for handling variable slice counts. It improved the average Dice score from 82.35% to 87.86% and drastically reduced the HD95 from 7.30 to 4.50, ensuring consistent anatomical representation.

Supplementary Table S6 Performance Impact of Volume Interpolation

Interpolation	Sagittal			Coronal			Average		
	IoU↑	Dice↑	HD95↓	IoU↑	Dice↑	HD95↓	IoU↑	Dice↑	HD95↓
N/A	67.43	80.03	9.07	73.59	84.67	5.52	70.51	82.35	7.30
YES	78.53	87.93	4.17	78.36	87.79	4.83	78.45	87.86	4.50

S7. Extended Results: Fracture Classification

S7.1. Ablation Study: Mixup Augmentation

To improve the generalization of the 2.5D Spatio-Sequential network, we incorporated Mixup augmentation. **Supplementary Table S7** details the ablation results, showing that Mixup significantly boosted all key metrics, including an increase in F1-Score from 61.61% to 66.54% and ROC-AUC from 88.33% to 90.19%.

Supplementary Table S7 Ablation Study on the usage of Mixup Augmentation.

Mixup Augmentation	Accuracy	Precision	Sensitivity	Specificity	F1-Score	ROC-AUC
Yes	93.54	72.16	62.31	97.09	66.54	90.19
No	92.32	63.00	60.41	95.95	61.61	88.33

S8. Interobserver Variability

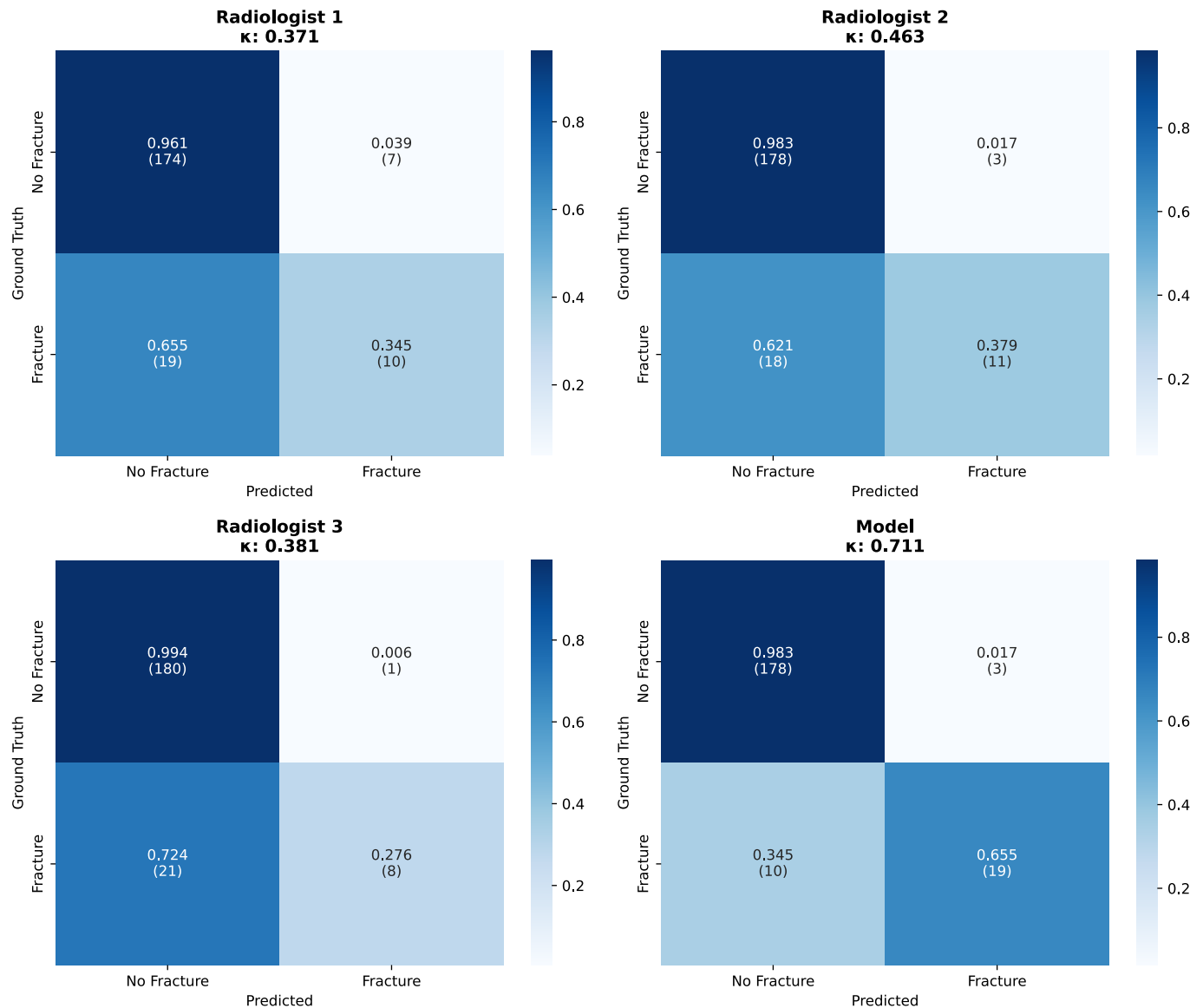
This subsection provides detailed visualizations of the agreement between the expert radiologists, the ground truth (GT), and our model.

Supplementary Figure S13 presents the pairwise Cohen's Kappa heatmaps. The analysis reveals that radiologists often had higher agreement with each other than with the ground truth, particularly for the difficult mid-cervical vertebrae (C3–C5). Radiologist 3 demonstrated the most distinct interpretive style, often showing lower agreement with peers.



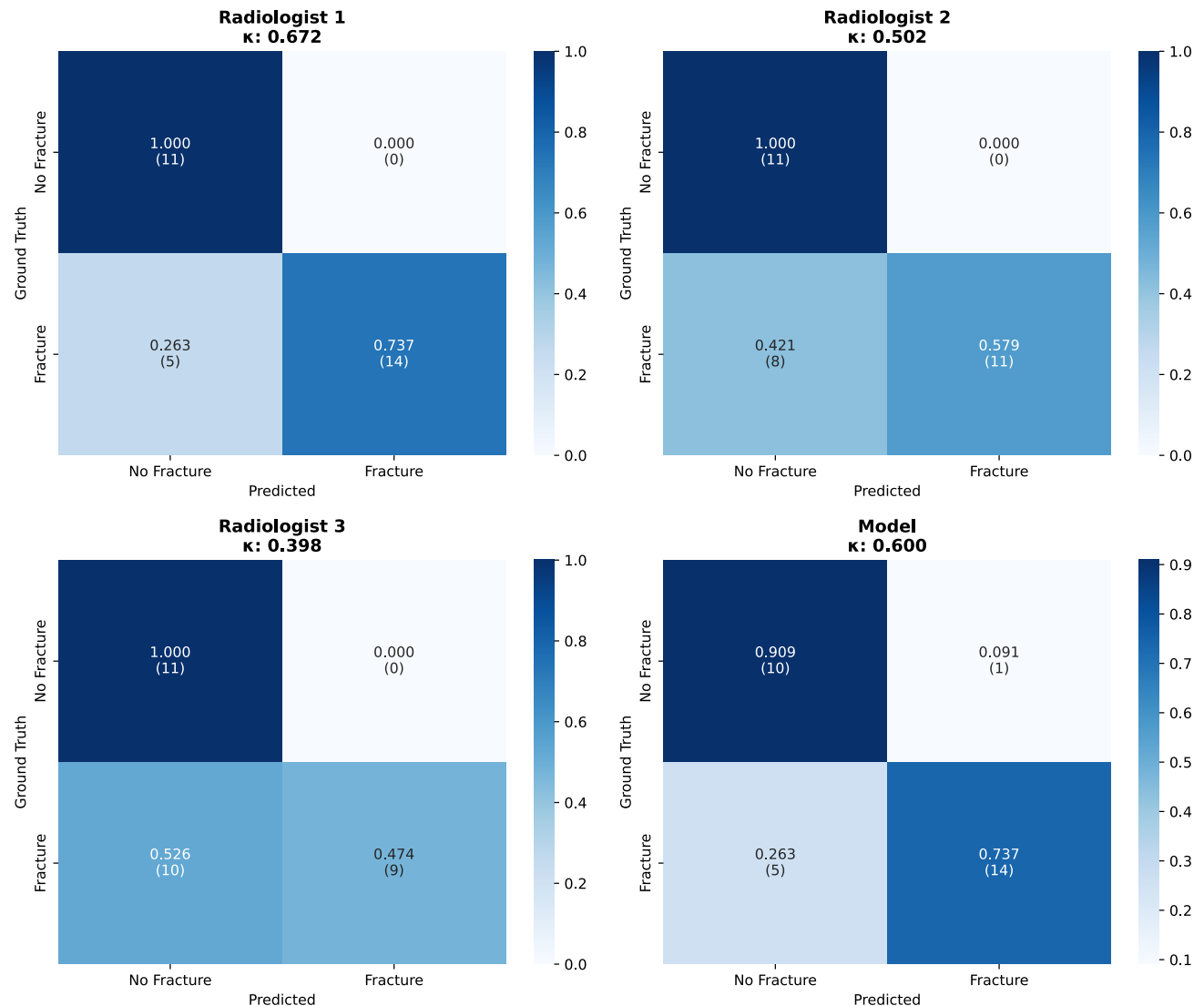
Supplementary Figure S13 Pairwise Cohen's Kappa Among 3 Radiologists and GT for All C1-C7 Vertebrae

Supplementary Figure S14 displays the confusion matrices for the model versus each radiologist against the ground truth at the vertebra level. The model correctly identified 19 of the 29 fractures in the test subset, whereas the radiologists identified 11, 11, and 8 respectively. This highlights the model's superior sensitivity in this challenging task.



Supplementary Figure S14 Confusion matrices comparing radiologist and model performance for cervical spine fracture detection at the vertebra level

Supplementary Figure S15 displays the confusion matrices at the patient level. The model correctly identified 14 of the 19 fractured patients, matching the performance of the best-performing radiologist (Radiologist 1) and outperforming the others.



Supplementary Figure S15 Confusion matrices comparing radiologist and model performance for cervical spine fracture detection at the patient level.